

Laboratory study of the collection efficiency of submicron aerosol particles by cloud droplets.

Part II - Influence of electric charges.

Alexis Dépée^{1,2}, Pascal Lemaître^{1*}, Thomas Gelain¹, Marie Monier^{2,3}, Andrea Flossmann^{2,3}

[1] {Institut de Radioprotection et de Sûreté Nucléaire (IRSN), PSN-RES, SCA, Gif-sur-Yvette, 91192, France}

[2] {Université Clermont Auvergne, Laboratoire de Météorologie Physique, Clermont-Ferrand, France}

[3] {CNRS, INSU, UMR 6016, LaMP, Aubière, France}

*Correspondence to: Pascal Lemaître (pascal.lemaitre@irsn.fr)

ABSTRACT

A new In-Cloud Aerosol Scavenging Experiment (In-CASE) has been developed to measure the collection efficiency (CE) of submicron aerosol particles by cloud droplets. Droplets fall at their terminal velocity through a one-meter-high chamber in a laminar flow containing aerosol particles. At the bottom of the In-CASE's chamber, the droplet train is separated from the aerosol particles flow and the droplets are collected in an impaction cup whereas aerosol particles are deposited on a High Efficiency Particulate Air (HEPA) filter. The collected droplets and the filter are then analysed by fluorescence spectrometry since the aerosol particles are atomised from a sodium fluorescein salt solution ($C_{20}H_{10}Na_2O_5$). In-CASE fully controls all the parameters which affect the CE - the droplets and aerosol particles size distributions are monodispersed, the electric charges of droplets and aerosol particles are known and set, while the relative humidity is indirectly controlled via the chamber's temperature. This paper details the In-CASE setup and the dataset of 70 measurements obtained to study the impact of the electric charges on CE. For this purpose, droplets and particles charges are controlled through two charging systems developed in this work - both chargers are detailed below. The droplet charge varies from $-3.0 \times 10^4 \pm 1.4 \times 10^3$ to $+9.6 \times 10^4 \pm 4.3 \times 10^3$ elementary charges while the particle charge ranges from zero to -90 ± 9 elementary charges depending on the particle radius. A droplet radius of $48.5 \pm 1.1 \mu\text{m}$ has been considered for four particle dry radii between 100 and 250 nm while the relative humidity level during experiments is $95.1 \pm 0.2 \%$. The measurements are then compared to theoretical models from literature - showing good agreement.

INTRODUCTION

Aerosol particles (APs) are a fundamental part of the atmosphere since they act on climate and more locally on meteorology (Twomey, 1974). They are also a key topic in human health where APs are known to increase the mortality (Dockery et al., 1992). For these reasons, the processes involved in the removing of the atmospheric AP have been investigated extensively over the last decades, through theoretical works (Slinn and Hales, 1971; Beard, 1974; Slinn, 1974; Young, 1974; Grover and Beard, 1975; Grover et al., 1977; Slinn, 1977; Davenport et al., 1978; Wang et al., 1978; Flossmann, 1998; Santachiara et al., 2012; Tinsley and Zhou, 2015; Cherrier et al., 2017; Dépée et al., 2019) as well as experimental measurements in lab (Kerker and Hampl, 1974; Wang and Pruppacher, 1977; Lai et al., 1978; Barlow and Latham, 1983; Pranesha and Kamra, 1996; Vohl et al., 2007; Ladino et al., 2011; Quérel et al., 2014; Ardon-Dryer et al., 2015; Lemaître et al., 2017; Dépée et al., 2020) and the environment (Volken and Schumann, 1993; Lasko et al., 2003; Chate and Pranesha, 2004; Depuydt, 2013; Laguionie et al., 2014). Far away from the source, APs are mainly scavenged through their collection by clouds and precipitations (Jaenicke, 1993) - referred as the wet deposition. Since it has been reported that the AP collection by clouds is dominated by wet deposition (Flossmann, 1998; Laguionie et al., 2014), the in-cloud AP collection remains an essential issue for the atmospheric sciences.

As previously stated in Part I of this work (Dépée et al., 2020) - « In most of current AP wet removal models - like DESCAM (Detailed SCAvenging Model, Flossmann, 1985) - the AP collection is described

50 through a microphysical parameter called “collection efficiency” (CE) which quantifies the ability of
51 a droplet to capture the APs present in its surroundings during its fall. It is the ratio between the AP
52 number (or mass) collected by the droplet over the AP number (or mass) within the volume swept by
53 the droplet for a given AP radius. Another equivalent definition is the ratio of the cross-sectional
54 area inside which the AP trajectories are collected by the droplet over the cross-sectional area of
55 the droplet.

56 Many microphysical effects influence this CE and their contribution is mainly depending on the AP
57 size. To be collected an AP has to deviate from the streamline around the falling droplet to make
58 contact with it. The nanometric AP’s trajectory is affected by the collisions with air molecules -
59 referred as the Brownian diffusion. It results in random movement patterns (see Figure 1, A) which
60 tend to increase the CE when the AP radius decreases. For massive APs, there is an increase of CE as
61 they retain an inertia strong enough to deviate significantly from the streamline when it curves and
62 to move straight toward the droplet surface - known as inertial impaction (see Figure 1, B). When
63 considering intermediate AP size, the CE goes through a minimum value called the “Greenfield gap”
64 (Greenfield, 1957) where the AP diffusion and inertia are weaker. In this gap, other microphysical
65 effects can be involved to make the droplet encounter the AP like the interception for instance. It is
66 the collection of APs following a streamline that approaches the droplet within a distance equivalent
67 to the particle radii (a) - see Figure 1, C». Note that there are also thermophoretic and
68 diffusiophoretic forces which can have an influence on the CE. These effects prevail in subsaturated
69 air - as it is the case sometimes in clouds - and are discussed in Part I (Dépée et al., 2020).

70 Since droplets are naturally charged in clouds (Takahashi, 1973) as well as the atmospheric APs, there
71 are electrostatic forces which can influence the AP collection. Numerous numerical studies were
72 dedicated to the influence of the electric charges on CE - such as Grover et al. (1975), Jaworek et
73 al. (2002), Tinsley and his group (for instance - Tinsley et al., 2006 or Tinsley and Zhou, 2015). They
74 suggest an increase of the CE of several orders of magnitude even when the AP is weakly charged.
75 However, the AP charge increases when the APs are radioactive (Clement and Harrison, 1992) -
76 inducing an impact on CE even larger (Dépée et al., 2019). Thus, the AP “electroscavenging” in clouds
77 has to be investigated, particularly for nuclear safety issues when the APs removal by clouds result
78 from the discharge of radioactive materials from a nuclear accident. For this purpose, the modelled
79 CEs with electrostatic forces need to be experimentally validated before the incorporation in cloud
80 models. Especially, the analytical expression for electrostatic forces used in numerical studies
81 (Jaworek et al., 2002 ; Tinsley et al., 2006 ; Tinsley and Zhou, 2015 ; Dépée et al., 2019) has to be
82 confirmed by measurements.

83 When a droplet with a charge Q approaches an AP of charge q , the partial influence of the AP
84 electrostatic field on the droplet leads to the re-orientation of the water dipoles. As a result, a
85 surface charge distribution on the droplet is created and supposed to be comparable to the one of a
86 conductive sphere. In an electrostatic equivalent problem, the droplet can be replaced by two point
87 charges (Jackson, 1999). One modelling the charge distribution, inside the droplet and near its
88 surface, another for the residual droplet charge located at the droplet surface. Finally, the analytical
89 expression of the electrostatic forces is the addition of two Coulomb forces between the AP and the
90 two-point charges inside the droplet. The factored expression can be found in equation (10) and
91 further details can be found in Tinsley et al. (2000). It consists of two terms. The first one is the
92 Coulomb inverse square term which prevails in the AP collection for large enough AP electrical
93 mobilities or electric charge products ($q \times Q$), attractive (Figure 1, D) or repulsive (Figure 1, E)
94 depending on whether the AP charge (q) and the droplet charge (Q) have unlike or like signs. The
95 second term is referred as the short-range attractive term and dominates for weak electric charge
96 products or for small AP electrical mobilities (Figure 1, F) and is always attractive (due to the charge
97 distribution at the droplet surface with opposite sign to the AP charge). A detailed study of their
98 contribution can be found in Tinsley and Zhou (2015) or Dépée et al. (2019).

99 Several laboratory studies investigated the influence of the electric charges on the CE (Beard, 1974;
100 Wang and Pruppacher, 1977; Lai et al., 1978; Barlow and Latham, 1983; Wang et al., 1983; Byrne and
101 Jennings, 1993; Lemaitre et al., 2020) - summarised in Table 1. However, most of these works have
102 faced difficulties in controlling all parameters impacting the CE. For instance, Beard (1974) did not
103 measure the AP charge; Lai et al. (1978) used a polydispersed AP size distribution, the relative
104 humidity level was not provided and the terminal velocity of the droplets was not reached ; Barlow
105 and Latham (1983) used a polydispersed AP size distribution and the relative humidity level
106 significantly varied from 50 to 70 % in their measurements; in the work of Byrne and Jennings (1993)
107 the droplet velocity does not reach the terminal velocity; the relative humidity measured in Lemaitre
108 et al. (2020) varied from 27 and 37 %. For these reasons, it is really difficult to find comparable CE
109 measurements in the literature as Barlow and Latham (1983) concluded after highlighting a

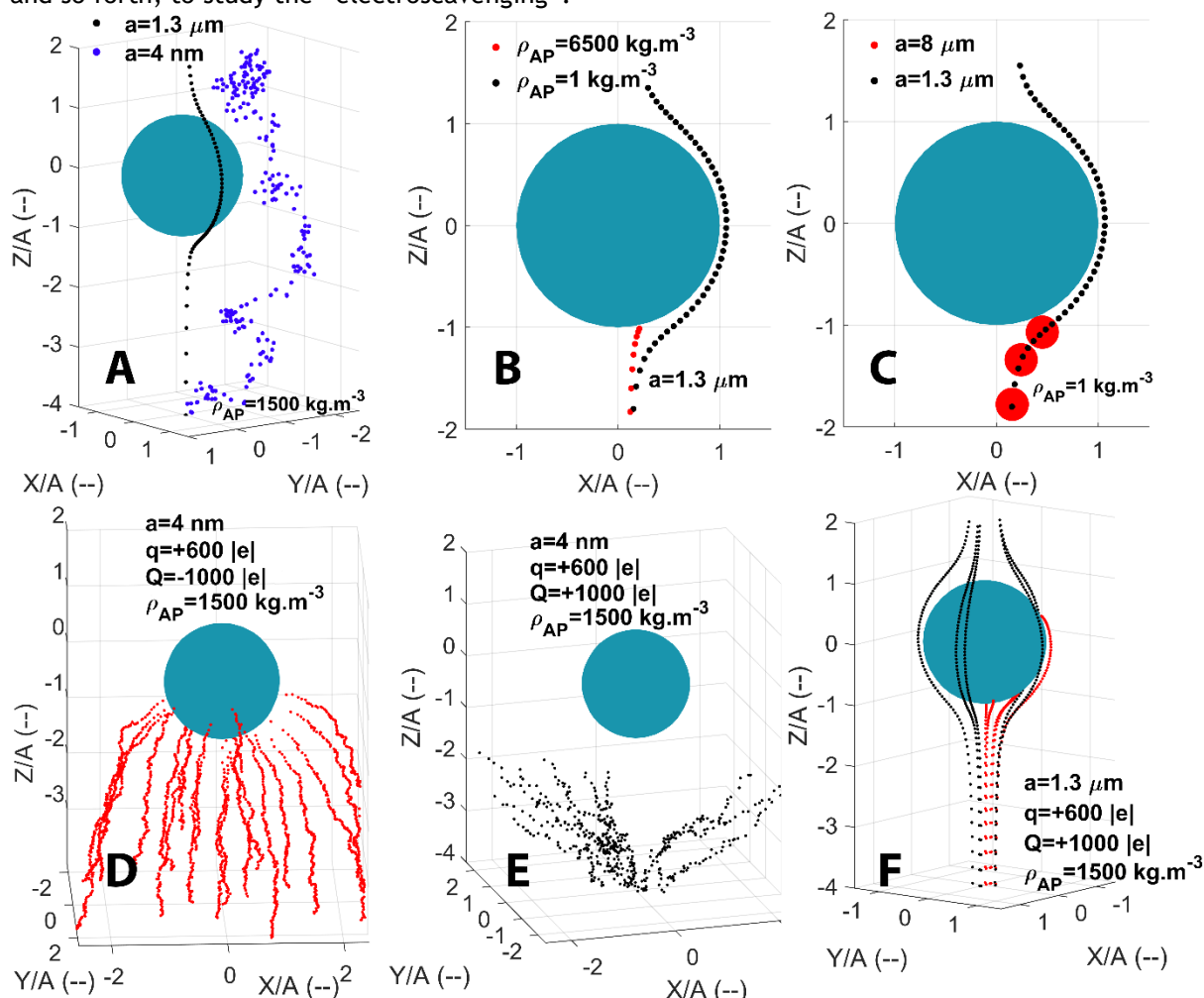
110 discrepancy of few orders of magnitude between all these authors. Nevertheless, Wang and
 111 Pruppacher (1977) and Wang et al. (1983) succeeded in controlling the charges and the sizes (as well
 112 as the relative humidity for Wang and Pruppacher (1977) but they considered only unlike signs
 113 between both droplets and APs. In their study, Lemaitre et al. (2020) did not observed any influence
 114 of electric charges on CE since for the low relative humidity level and the large droplet radius
 115 considered, the diffusiophoretis and thermophoresis dominated the AP collection.
 116 Thus, only the Coulomb inverse square term in the analytical expression of the electrostatic forces
 117 can be documented whereas the contribution of the short-range attractive term has not been
 118 experimentally verified until now.

119
 120 Table 1 Laboratory studies focused on the influence of electric charges on the CE. Charges are
 121 presented in number of elementary charges.

Parameter Study	Droplet radius (μm)	AP radius (μm)	Droplet charge ($ e $)	AP charge ($ e $)	Relative humidity (%)	Terminal velocity
Beard (1974)	200 - 425	Monodisperse 0.35-0.44 ± 0.04	$10^4 - 10^6$	Not measured	99	Reached
Wang and Pruppacher (1977)	170 - 340	Monodisperse 0.25 ± 0.03	10^6	9 & 15 ± 2	23 ± 2	Reached
Lai et al. (1978)	620 & 820	Polydisperse 0.15 - 0.45	$10^7 - 10^8$	Not measured	Neither controlled nor measured	Not reached
Barlow and Latham (1983)	270 - 600	Polydisperse 0.2 - 1	$10^4 - 10^7$	Neutralised	Uncontrolled but measured 50 - 70	Reached
Wang et al. (1983)	69 - 250	Monodisperse 0.038 - 0.1	$10^7 - 10^8$	1 - 13.5	Uncontrolled	Reached
Byrne and Jennings (1993)	400 - 500	Monodisperse 0.35 - 0.88	$10^5 - 10^8$	360 - 750	57	Not reached
Lemaitre et al. (2020)	1275	Polydisperse 0.15 and 0.25	$10^5 - 10^8$	Neutralised and measured (0 ± 0.1)	Uncontrolled but measured 27 - 37	Reached

122
 123 The purpose of this study is to overcome this lack of data by providing new CE measurements for
 124 weakly and strongly droplets and APs charges with both negative and positive charge products, to
 125 quantify the effect of the short-range attractive term on the CE since its contribution was previously
 126 predicted by modelling (Tinsley and Zhou, 2015; Dépée et al., 2019).
 127 Thus, a novel experiment has been designed to study the influence of electric charges on the CE
 128 which is presented in this paper. Note that this experiment was also used to study the influence of
 129 relative humidity which is the object of the companion paper: Part I (Dépée et al., 2020).
 130 The first part of the paper describes the experimental setup. Afterwards, the method to evaluate
 131 the CE and the uncertainties are detailed. Then, the measurements are presented and confronted
 132 with the prediction of Kraemer and Johnstone (1955) and the Lagrangian model of Dépée et al.
 133 (2019). Finally, this work concludes with the experimental validation of the Dépée et al. (2019) model

134 and a necessary incorporation of the modelled CEs in cloud models, pollution models, climate models,
 135 and so forth, to study the “electroscavenging”.



136
 137 Figure 1 APs trajectories computed with the extended Dépée et al. (2019) model for a 50 μm droplet
 138 radius (A) and AP with various radii (a) and densities (ρ_{AP}). The air temperature (T_{air}) and the air
 139 pressure (P_{air}) are -17°C and 540 hPa, respectively. The panels indicate the effects of Brownian
 140 motion (A), inertial impact (B), interception (C), electrostatic forces with attractive (D) and repulsive
 141 (E, F) Coulomb forces. Red trajectories result in an AP collection. The droplet (Q) and AP (q) charges
 142 are labelled. In Figures 1 B to F - the red trajectories result in an AP collection. Adapted from Part I
 143 (Dépée et al., 2020).

144
 145

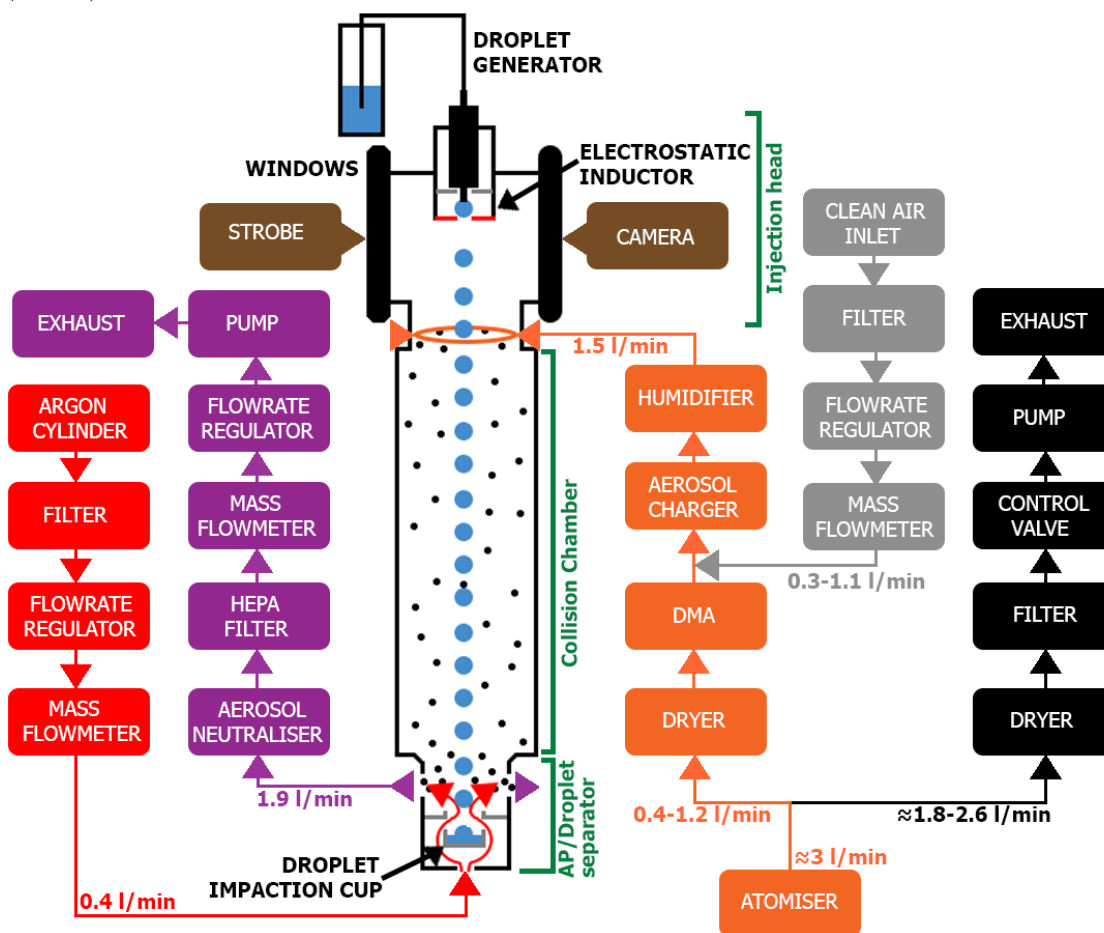
1 EXPERIMENTAL SETUP

1.1 Overview

148 Figure 2 shows the In-Cloud Aerosol Scavenging Experiment (In-CASE) which has been built to study
 149 the influence of the electric charges on the CE. Droplets fall at their terminal velocity (≈ 25 cm/s)
 150 into a chamber through an AP flow of 1.5 l/min. The flow velocity is 1.3 cm/s and the AP transfer
 151 time in the collision chamber is almost 80 s. The In-CASE's chamber is subdivided into 3 parts - the
 152 injection head where droplets and APs are inserted; the collision chamber where droplets and APs
 153 interact with each other; the aerodynamic separator set at the bottom's chamber impacts droplets
 154 into an impaction cup while uncollected APs pass out of the chamber toward a High Efficiency
 155 Particulate Air (HEPA) filter. For this latter stage, an Argon updraft assures that there are no AP that
 156 settle into the droplet impaction cup. More details on the In-CASE's chamber can be found in section
 157 1.2 of Dépée et al. (2020).

158 APs are atomised from a sodium fluorescein salt solution ($C_{20}H_{10}Na_2O_5$). This molecule has been
 159 used for its significant fluorescent properties, detectable at very low concentrations (down to 10^{-10}
 160 g/l). Once generated, the APs flow through a diffusion dryer and a portion of the flow is then directed
 161 into a Differential Mobility Analyser (DMA; TSI 3080) to select APs following their electrical mobilities

162 whereas the overflow ends in an exhaust (black, Figure 2). At the DMA's outlet, the AP size
 163 distribution is assumed to be monodispersed (discussed in section 2.1). Thereafter, APs are
 164 electrically charged by a custom-designed field charger (section 1.4). Since the optimised AP flowrate
 165 in the charger is 1.5 l/min and the maximum AP flowrate in the DMA was 1.2 l/min during the
 166 experiments, a clean air flowrate is added at the charger's inlet. Before the AP injection in the In-
 167 CASE's chamber, the flow is humidified to ensure a high relative humidity level inside the collision
 168 chamber (section 1.2). Thus, the hygroscopicity of the sodium fluorescein salt is considered during
 169 the experiments (see section 2.2). Before the AP collection on the HEPA filter, the APs flow through
 170 a low-energy X-ray neutraliser (< 9.5 keV, TSI 3088) to eliminate charge accumulation on this filter
 171 leading to AP deposition on the metallic walls of the filter holder. Note that the pipes are anti-static
 172 and connected to the ground (as well as the collision chamber) so there is no accumulation charge
 173 before the HEPA filter due to AP deposition.
 174 Droplets are generated with a piezoelectric injector provided by Microfab (MJ-ABL-01 model) with an
 175 internal diameter of 150 μm - at 25 Hz to prevent droplets from coalescing. The generator is set
 176 in a housing made with a 3D printer which is located in the injection head (Figure 5, Right). An
 177 electrostatic inductor is also placed in the housing to charge droplets (section 1.5). The droplet size
 178 is measured during experiments by optical shadowgraphy (with a strobe and a camera, brown color
 179 in Figure 2) through two opposite windows in the injection head. Further details can be found in
 180 section 1.4 of *Dépée et al. (2020)* but note that the size distributions of the droplets generated by
 181 the piezoelectric injector are considered monodispersed since the droplet size dispersion is very low
 182 ($\sigma \sim 1\%$).



183 Figure 2 In-CASE setup to study the electric charges' influence - adapted from Part I (*Dépée et al.,*
 184 *2020*). Colors represent different functions. Red - upward argon flow against AP pollution in
 185 the droplet impaction cup. Purple - AP (and Argon) evacuation toward the HEPA filter after
 186 neutralisation. Orange - AP, generation, selection and charging. Black - surplus evacuation
 187 and DMA flowrate control. Grey - clean air adding for a constant flowrate at the AP charger's
 188 inlet. Brown - droplet radius measurement.

190
 191 **1.2 Thermodynamic conditions in the In-CASE's chamber**

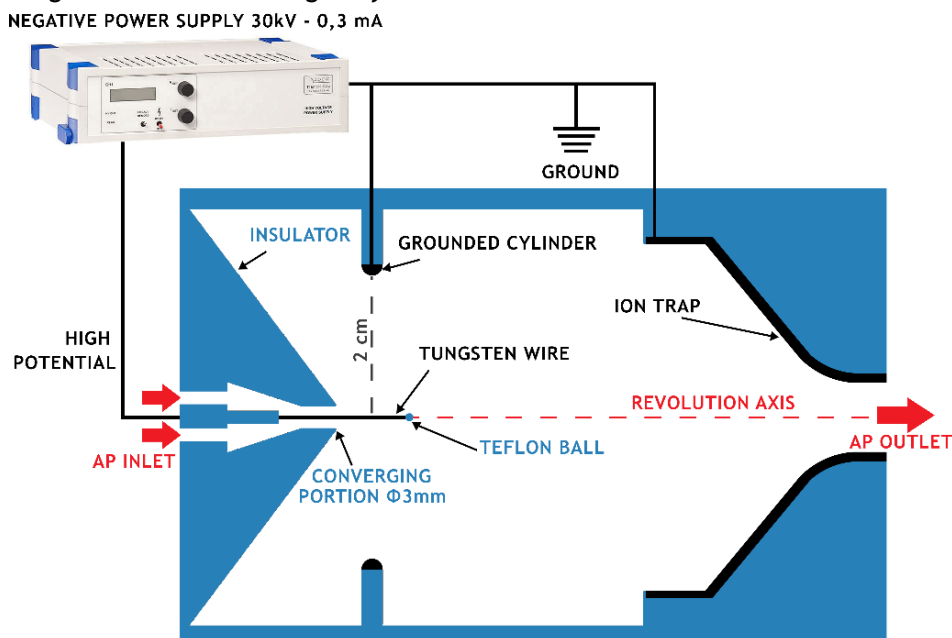
192 Thermodynamic conditions were set as constant as possible during experiments to get comparable
 193 CE measurements. The pressure in the In-CASE's chamber was one atmosphere and the mean
 194 temperature for the campaign presented in this paper was 1.08 ± 0.12 °C. As referred in section 1.2
 195 of **Dépée et al. (2020)**, the chamber's temperature is controlled through a cooling system which
 196 indirectly sets the relative humidity level in the chamber. Here, the temperature of the pure water
 197 in the humidifier placed before the In-CASE's chamber (Figure 2) was increased to get a mean relative
 198 humidity level in the chamber of 95.1 ± 0.2 %. Note that this relative humidity level was the maximum
 199 which could be reached with In-CASE. In this way, the contribution of the thermophoretic and the
 200 diffusiphoretic effects in the CE measurements were reduced as much as possible.

202 1.3 Droplet evaporation

203 The droplet evaporation was theoretically evaluated through the section 13.2 of Pruppacher and Klett
 204 (1997). The terminal velocity of the droplet ($U_{A,\infty} \approx 25$ cm/s) is computed from Beard (1976)
 205 meanwhile the droplet residence time in the collision chamber (≈ 4 s) is deduced from the changes in
 206 droplet radius and terminal velocity. For a relative humidity level of 95 %, it was found that the
 207 droplet radius decreases by less than 0.3 % from the droplet generation to the bottom of the collision
 208 chamber. Thus, the droplet evaporation in the In-CASE collision chamber was neglected for the
 209 discussions below.

213 1.4 AP charging

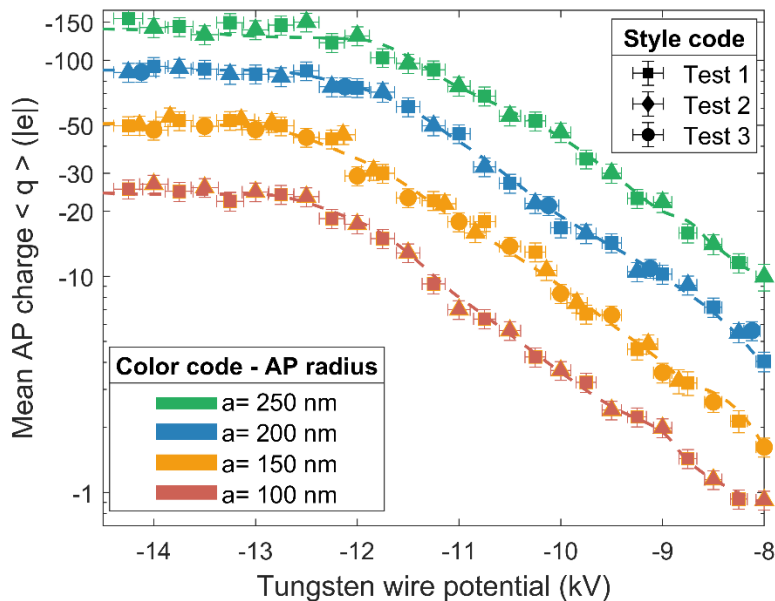
214 APs are electrically charged by passing through a custom-designed field charger adapted from Unger
 215 et al. (2004). The scaled geometry is presented in Figure 3. This charger is based on a system of
 216 electric discharges produced between a high potential tungsten wire and a grounded cylinder. A
 217 metallic converging portion is used at the charger's outlet to trap ions and ensure only charged APs
 218 can leave the charger. A Teflon ball ($\varnothing=1$ mm) is set at the end of the tungsten wire to ensure there
 219 is no point effect between the wire and the ion trap. A large number of ions are then created and
 220 migrate between the two centimeters interelectrode space along the electric field lines. Finally, the
 221 APs flow through them and are charged by ion attachment.



222
 223
 224 Figure 3 Geometry of the home-made AP charger based on Unger et al. (2004) (at scale).
 225

226 The charging relationships of the charger used during all experiments are presented in Figure 4. They
 227 provide the mean electric AP charge related to the potential at the tungsten wire for the 4 AP radii
 228 considered here. It results from *ex situ* experiments which are detailed in Appendix A. Note that APs
 229 are negatively charged through the discharge regime used (negative Trichel regime) and there is an
 230 electric potential where the AP charge saturates which is typical for field chargers (Pauthenier and
 231 Moreau-Hanot, 1932). These results were performed at an AP flowrate of 1.5 l/min which was found

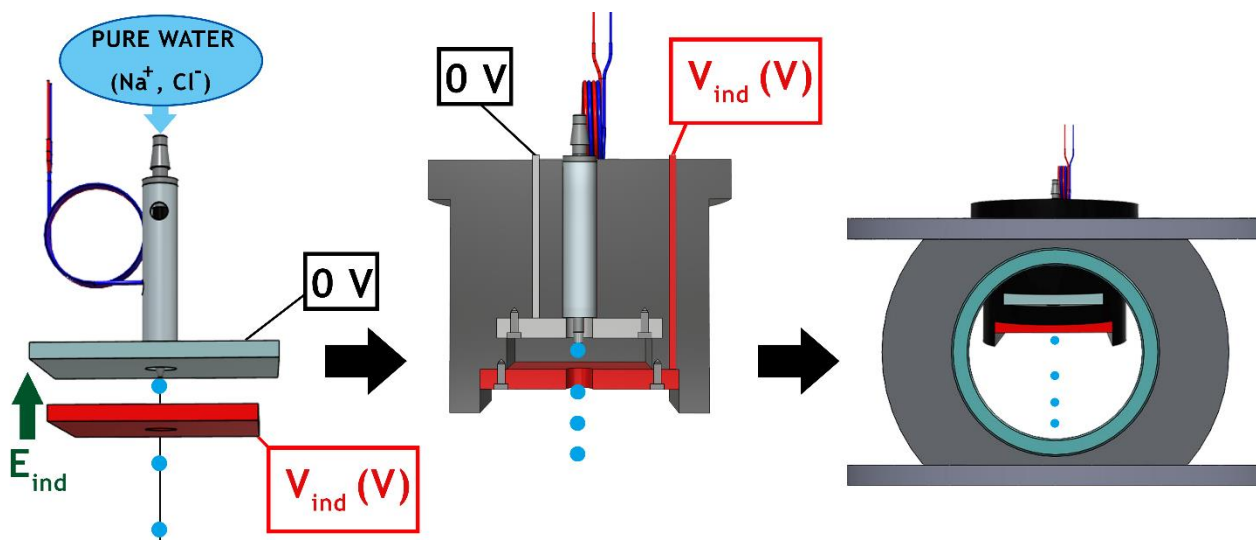
232 to maximise the AP penetration inside the charger and consequently the AP concentration inside the
 233 In-CASE's chamber. Penetration tests - not presented in this study - were deduced by varying the AP
 234 flowrate in the setup detailed in Appendix A.



235
 236
 237 Figure 4 AP charging relationships used during experiments for the 4 AP radii (a) considered. Error
 238 bars represent the standard deviations in measurements.
 239

240 1.5 Droplet charging

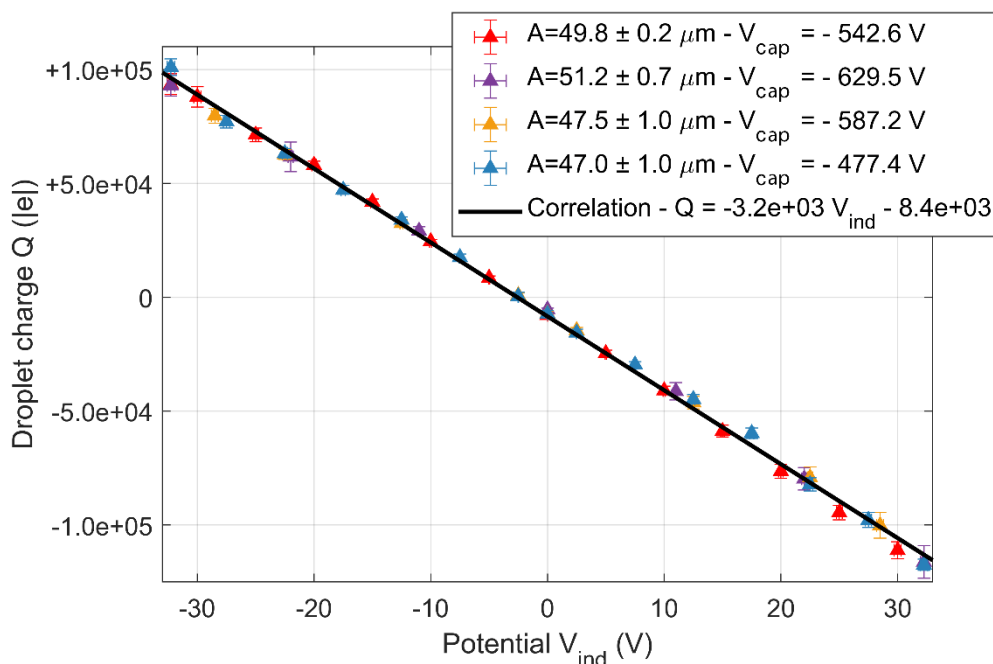
241 The droplets charge is controlled through an electrostatic inductor adapted from Reischl et al. (1977).
 242 Two parallel metallic plates are set at the droplet generator's nozzle (Figure 5, left) - one plate
 243 connected to the neutral potential and the other one to a potential referred as V_{ind} . It induces an
 244 electric field ($E_{ind} \sim 10^2 - 10^3$ V/m) at the nozzle. Since sodium chloride is added to the pure water that
 245 feeds the piezoelectric droplet generator, this electric field can selectively attract negative or
 246 positive ions toward the nozzle where the droplet is formed, according to its sign. If V_{ind} is negative,
 247 the positive sodium ions (Na^+) migrate toward the nozzle and the negative chloride ions (Cl^-)
 248 are repulsed from the nozzle and inversely if the potential is positive. Furthermore, the amplitude of the
 249 electric field (E_{ind}) sets the ion quantity in the droplet. Note that the sodium chloride concentration
 250 has no impact on the induced droplet charge if the ion number is large enough for the entire
 251 experiment time (Reischl et al., 1977) - 3.3 g/l was used here.
 252



253
 254

255 Figure 5 (Left) Electrostatic inductor below the piezoelectric droplet generator. (Center) Cross
 256 section of the housing made with a 3D printer that hold the droplet generator. (Right) Injection head
 257 at the top of the In-CASE's chamber containing the housing made with a 3D printer.
 258

259 A method to evaluate the droplet charge was developed in this study and is detailed in Appendix B.
 260 In Figure 6, the resulting charging relationship of the electrostatic inductor is presented. It gives the
 261 droplet charge (Q) as a function of the electrostatic inductor potential (V_{ind}). We note that the
 262 droplet generator produces highly electrically charged droplets since the droplet charge is evaluated
 263 to about -8,400 elementary charges, for a zero potential at the inductor plate ($V_{ind} = 0$ V). This is in
 264 line with Ardon-Dryer et al. (2015) which used a similar generator and measured up to 10^4 elementary
 265 charges on the generated droplets. Finally, this charging relationship is used during experiments to
 266 positively or negatively set the droplet charges. The electrostatic inductor and the droplet generator
 267 are placed into a housing made with a 3D printer (Figure 5, center), this latter being placed in the
 268 injection head at the top of the In-CASE's chamber (Figure 5, right).



269
 270
 271 Figure 6 Droplet charge versus electrostatic inductor voltage. The colours identify different tests
 272 performed to ensure there is no droplet charge modification over time and manipulations. Error bars
 273 represent the standard deviation of the droplet radii evaluated. The parameter V_{cap} is the potential
 274 at the capacitor to measure the droplet charge. Note that the radius of the droplet is deduced from
 275 the reversed Beard (1976) model and its terminal velocity - this latter being measured by optical
 276 shadowgraphy. See Appendix B for more further details.
 277

278 2 DATA ANALYSIS

279 2.1 Assumption of a monodispersed AP size distribution

281
 282 As a reminder, APs flow through a DMA (Figure 2) to select APs following their electrical mobility. As
 283 explained in section 2.2 of the Part I (Dépée et al., 2020), several AP radii can actually be selected
 284 depending on their elementary charges given that they have the same electrical mobility. For
 285 example, with a selected AP radius of 100 nm at the DMA (considering one elementary charge on it),
 286 the doubly-charged AP radii of 161.8 nm will also be selected.
 287

288 Sometimes, the multiple charged APs cannot be neglected in the AP flow at the DMA's outlet. The
 289 CE deduction is then more difficult (Dépée et al., 2020). Here, the aerodynamic impactor at the
 290 DMA's inlet as well as the AP flowrate in the DMA were optimised to prevent double (and greater)
 291 charged AP from being selected by the DMA. Indeed, the cut-off radius of the impactor at the DMA's
 292 inlet (referred as $D_{50\%/2}$) - which is the radius where 50 % of the APs are impacted - is small enough

293 compared to the double charged AP radius. This is summarised in Table 2 for all selected AP radii
 294 used in the experiments. Thus, the AP size distribution at the DMA's outlet is assumed to be
 295 monodispersed and the CE is deduced as follows.

296 Table 2 AP selection parameters

Selected dry AP radius by the DMA (single charged)	Double charged dry AP radius with the same electrical mobility	AP flowrate in the DMA	Cut-off radius of the impactor at the DMA's inlet ($D_{50\%}/2$)
100 nm	161.8 nm	1.2 l/min	140 nm
150 nm	253.7 nm	1.0 l/min	157 nm
200 nm	348.3 nm	0.6 l/min	213 nm
250 nm	444.3 nm	0.4 l/min	268.5 nm

297

298 2.2 Collection efficiency definition

299

300 The collection efficiency (CE) is calculated from the equation (1):

$$CE(a, A, q, Q, HR) = \frac{m_{AP,d}}{m_{AP,available}} \quad (1)$$

301 Where $m_{AP,d}$ is the AP mass collected by all droplets which is directly measured by fluorescence
 302 spectrometry analysis of the droplets collected in the impaction cup, which is located at the bottom
 303 of the In-CASE chamber (Figure 4 of [Dépée et al., 2020](#)). $m_{AP,available}$ is the mass of available APs in
 304 the volume swept by all droplets - evaluated with the equation (2) :

$$m_{AP,available} = \pi(A + GroF(RH) \times a)^2 \times F_d \times \Delta t \times H_{eff} \times C_{m,AP} \quad (2)$$

305 With A - the droplet radius, F_d - the droplet generation frequency, Δt - the experiment duration (from
 306 3 to 6 hours), a - the AP dry radius, $C_{m,AP}$ - the mean AP mass concentration in the In-CASE collision
 307 chamber, $GroF$ - the growth factor of AP depending on the relative humidity (RH). This latter
 308 characterises the hygroscopicity of the sodium fluorescein salt - further details related to its
 309 evaluation can be found in section 1.2.3.3 of [Dépée et al. \(2020\)](#). H_{eff} is the effective height of
 310 interaction between APs and droplets calculated with the equation (3):

$$H_{eff} = \frac{U_{A,\infty}}{U_{A,\infty} + V_Q} H_{In-CASE} \quad (3)$$

311 With the AP flow velocity (V_Q) equal to 1.3 cm/s (for an AP flowrate of 1.5 l/min), the droplet
 312 terminal velocity ($U_{A,\infty}$) assumed to be equal to 25 cm/s and the In-CASE collision chamber's height
 313 ($H_{In-CASE}$) of 1 meter.

314

315 In equation (2), the mean AP mass concentration ($C_{m,AP}$) in the In-CASE collision chamber is evaluated
 316 from the fluorescence spectrometry analysis of the HEPA filter. It is given by the equation (4) where
 317 $Q_{In-CASE,c}$ is the AP flowrate going through the In-CASE collision chamber and $m_{AP,tot}$ is the total AP
 318 mass on the HEPA filter at the end of the experiment.

319

$$C_{m,AP} = \left(1 + \frac{1 - P_{InCASE,a,q}}{2}\right) \frac{m_{AP,tot}}{\Delta t \times Q_{In-CASE,c}} \quad (4)$$

320 The mean AP mass concentration is corrected considering the penetration ($P_{InCASE,a,q}$) in the collision
 321 chamber which depends on the AP radius (a) and charge (q). This parameter was estimated during
 322 *ex situ* experiments where the setup was the same as Figure 2, the only difference being a
 323 Condensation Particle Counter (CPC) positioned behind the AP neutraliser and the AP charger to
 324 measure two AP number concentrations, n_1 and n_2 , respectively. The penetration is then defined as
 325 concentration n_1 over concentration n_2 . Thus, the measured penetration accounts for the AP

326 deposition due to electrostatic forces on the wall of the collision chamber as well as in the pipes
 327 from the AP charger to the HEPA filter and the humidifier (Figure 2). The measured penetrations are
 328 presented in Table 3. It is observed that the penetration decreases when the AP charges (q) increase
 329 and the AP radius (a) decreases since the electrical mobility of APs is larger. During experiments, the
 330 AP number concentration ranged from $3 \times 10^4 \text{ cm}^{-3}$ (for $a=100 \text{ nm}$ and $= -10 \pm 1 |e|$) to $2 \times 10^3 \text{ cm}^{-3}$
 331 (for $a=250 \text{ nm}$ and $q = -90 \pm 9 |e|$). As a reminder, the pipes are anti-static and connected to the
 332 ground (as well as the collision chamber) so there is no charge accumulation due to AP deposition
 333 during experiments. Thus, the penetrations presented in Table 3 are assumed to be constant over
 334 time. Note that the AP deposition was neglected in Part I (Dépée et al., 2020) since the penetration
 335 was almost 100 % when the APs are neutralised.

336
337
338
339 Table 3 Measured penetration for the experimental conditions.

Dry AP radius (a)	AP charge (q)	Penetration ($P_{\text{InCASE},a,q}$)
100 nm	$-10 \pm 1 e $	94.7 %
	$-20 \pm 2 e $	86.0 %
150 nm	$-11 \pm 1 e $	96.5 %
	$-30 \pm 3 e $	86.2 %
200 nm	$-10 \pm 1 e $	97.0 %
	$-34 \pm 3 e $	88.8 %
	$-71 \pm 7 e $	78.2 %
250 nm	$-22 \pm 2 e $	94.1 %
	$-52 \pm 5 e $	89.6 %
	$-90 \pm 9 e $	81.8 %

340
341
342
343
344
345
346
347
348

2.3 Uncertainties

The relative CE uncertainty (u_{CE}) is calculated following Lira (2003) and presented in equation (5):

$$u_{CE} = \sqrt{u_A^2 + u_{H_{eff}}^2 + u_{N_d}^2 + u_{m_{AP,d}}^2 + u_{C_{m,AP}}^2} \quad (5)$$

349 where the relative uncertainties are related to the droplet radius ($u_A \approx 1\%$), the effective height of
 350 interaction between droplets and APs ($u_{H_{eff}} \approx 4\%$), the number of injected droplets during the
 351 experiment ($u_{N_d} \approx 2\%$), the measured AP mass in the droplet impaction cup ($u_{m_{AP,d}}$) and the mean AP
 352 mass concentration in the In-CASE collision chamber during the experiment ($u_{C_{m,AP}}$).

353 The relative uncertainty $u_{m_{AP,d}}$ is evaluated through the equation (6) :

$$u_{m_{AP,d}} = \sqrt{u_{fluorimeter}^2 + u_{dilution}^2} \quad (6)$$

354 where $u_{dilution}$ is the relative uncertainty of the dilution performed during the spectrometry analysis,
 355 assumed to be equal to 1 %, and $u_{fluorimeter}$ is the relative uncertainty of the fluorimeter which can
 356 be up to 30 % when the measured AP mass is close to the detection limit. The relative uncertainty of
 357 the mean AP mass concentration in the In-CASE collision chamber ($u_{C_{m,AP}}$) is calculated through the
 358 equations (7) :
 359

$$\begin{cases} u_{C_{m,AP}} = \sqrt{u_{m_{AP,tot}}^2 + u_{Q_{In-CASE,c}}^2 + u_{\Delta t}^2 + u_p^2} \approx \sqrt{u_{m_{AP,tot}}^2 + u_{Q_{In-CASE,c}}^2 + u_p^2} \\ u_{m_{AP,tot}} = \sqrt{u_{fluorimeter}^2 + u_{dilution}^2} \end{cases} \quad (7)$$

360 $u_{m_{AP,tot}}$ is the relative uncertainty of the measured AP mass on the HEPA filter which depends on the
 361 relative uncertainties of the dilution ($u_{dilution} \approx 1\%$) and the fluorimeter ($u_{fluorimeter} \leq 30\%$) - $u_{Q_{In-CASE,c}}$
 362 is the relative uncertainty of the AP flowrate in the collision chamber equal to 1% - $u_{\Delta t}$ is the relative
 363 uncertainty of the experiment duration which is neglected here. More details are addressed in Part I,
 364 section 2.3 (Dépée et al., 2020) where the same definitions are used, except the relative uncertainty
 365 of the AP penetration in the collision chamber (u_p) is added here (equation (8)).

$$u_p = \frac{1 - P_{InCASE,a,q}}{2} \quad (8)$$

366 As mentioned in 3.2.3.2, an AP pollution independent from the experiment (pollution during the
 367 spectrometry analysis, when the droplet impaction cup is extracted at the end of experiments, etc.)
 368 remains and should be considered in equation (5). Indeed, it can significantly increase the CE
 369 measurement, especially when the measured AP mass is close to the detection limit of the
 370 fluorescence spectrometer. Considering the experiment duration (< 6 hours), this pollution is not
 371 totally negligible for CEs below 1×10^{-4} . Rather than discarding these measurements, their low
 372 uncertainty were extended down to the lower limit of the axis in Figures 7 and 10.

374 Also, we assume that APs have the same charge (q). Even if, an AP charge distribution exists, this
 375 contribution is negligible. Nevertheless, the AP charge distribution was not measured here.

376
377

378 3 RESULTS AND DISCUSSIONS

379

380 3.1 Extension of the Dépée et al. (2019) model

381 CE measurements are compared to the model of Dépée et al. (2019) which models the electrostatic
 382 forces (F_{elec}) between droplets and APs in the CE calculation. Since all experiments were performed
 383 in subsaturated air ($RH = 95.1 \pm 0.2\%$), the thermophoretic (F_{th}) and the diffusio-phoretic (F_{df}) forces
 384 were also considered for the comparison with the model. Indeed, Dépée et al. (2020) showed that
 385 the contribution of these two effects is significant even though the relative humidity is close to 100%.
 386 Thus, the Dépée et al. (2019) model is extended here by replacing the resulting velocity at the AP
 387 location ($\mathbf{U}_{f@p}$ in their Equation 6) by the equation (9):

$$\mathbf{U}_{f@p}^*(t) = \mathbf{U}_{f@AP}(t) + \frac{\tau_{AP}}{m_{AP}} (\mathbf{F}_{buoy} + \mathbf{F}_{df} + \mathbf{F}_{elec} + \mathbf{F}_{th}) \quad (9)$$

388 Where $\mathbf{U}_{f@AP}$ is the fluid velocity at the AP location, τ_{AP} the AP relaxation time and m_{AP} the AP mass.
 389 The expression of the buoyancy force (F_{buoy}) is detailed in equation system (B.1), F_{df} and F_{th} in the
 390 equations (12) of Dépée et al. (2020). F_{elec} is defined in equation (10) :

391

$$\mathbf{F}_{elec} = \frac{q^2}{4\pi\epsilon_0 A^2} \left[\overbrace{\left(-\frac{r^*}{(r^{*2} - 1)^2} + \frac{1}{r^{*3}} \right)}^{\text{Short-range attractive term}} + \underbrace{\frac{1}{r^{*2}} \times \frac{Q}{q}}_{\text{Coulomb inverse square term}} \right] \mathbf{u}_r \quad (10)$$

392

393 With ϵ_0 - the permittivity of the free space, \mathbf{u}_r - the unit vector in the radial direction from the
 394 droplet centre to the AP centre, r^* - the distance between the AP and droplet centres, normalised
 395 by the droplet radius A .

396

397 Note that radioactive APs are known to get positively charged (Clement and Harrison, 1992) whereas
 398 the APs were negatively charged in this work (Figure 4), through the charging regime used in the AP
 399 charger (for integrity of the tungsten wire over time). Nevertheless, since we have the relation
 400 $F_{elec}(q, -Q) = F_{elec}(-q, Q)$ in equation (10), the CE measurements with the same $\frac{q}{Q}$ ratios are
 401 equivalent, assuming this analytical expression is validated by the measurements (see section 3.2.3).
 402
 403

404 **3.2 Collection efficiency measurements**

405 The CE measurements for various charges are presented in Table 4 for the 4 wet AP radii (a_{wet})
 406 considered in this study. Note that the wet AP radii are the ones of the APs which grew in the collision
 407 chamber due to their hygroscopicity. During experiments, the AP radius increases by a growth factor
 408 ($GroF$) between 1.73 and 1.75 (since we actually considered the 4 mean levels of relative humidity
 409 for the 4 AP radii used in the experiments). Further details related to the calculation of the growth
 410 factor can be found in section 1.2.3.3 of Dépée et al. (2020). In Table 4, the droplet (Q) and AP (q)
 411 charges are also informed by number of elementary charges. The mean temperature was $1.08 \pm$
 412 0.12°C and the mean relative humidity was $95.1 \pm 0.2\%$ for a droplet radius of $48.5 \pm 1.1\ \mu\text{m}$. Note
 413 that the wet AP density depends on the one of sodium fluorescein salt and water. The equation (1)
 414 of Dépée et al. (2020) yielded a density of $1110\ \text{kg}\cdot\text{m}^{-3}$. The key features of the experiments are
 415 summarised in Table 5.

416
417
418 Table 4 CE measurements

a_{wet} (nm)	$Q(e)$ $q(e)$	$9.6 \times 10^4 \pm 4.3$	3.0×10^4	5.0×10^3	$0 \pm 6.0 \times 10^2$	-5.0×10^3	-1.0×10^4	-3.0×10^4
		$\times 10^3$	$\pm 1.9 \times 10^3$	$\pm 8.4 \times 10^2$		$\pm 7.7 \times 10^2$	$\pm 8.7 \times 10^2$	$\pm 1.4 \times 10^3$
175 ± 3	-10 ± 1	3.91×10^{-2}	2.44×10^{-2}	3.47×10^{-3}	4.17×10^{-3}	5.58×10^{-3}	9.81×10^{-4}	2.55×10^{-4}
	-20 ± 2	6.77×10^{-2}	3.47×10^{-2}	6.99×10^{-3}	5.07×10^{-3}	4.25×10^{-3}	9.17×10^{-4}	4.12×10^{-5}
260 ± 3	-11 ± 1	2.41×10^{-2}	1.30×10^{-2}	3.25×10^{-3}	2.97×10^{-3}	2.14×10^{-3}	1.34×10^{-3}	1.93×10^{-4}
	-30 ± 3	7.91×10^{-2}	2.31×10^{-2}	7.96×10^{-3}	5.75×10^{-3}	3.47×10^{-3}	2.57×10^{-3}	4.97×10^{-5}
346 ± 4	-10 ± 1	2.24×10^{-2}	8.98×10^{-3}	3.03×10^{-3}	1.86×10^{-3}	1.84×10^{-3}	1.05×10^{-3}	5.20×10^{-4}
	-34 ± 3	4.58×10^{-2}	1.40×10^{-2}	5.39×10^{-3}	3.91×10^{-3}	2.90×10^{-3}	2.23×10^{-3}	3.60×10^{-5}
	-71 ± 7	9.17×10^{-2}	3.25×10^{-2}	1.70×10^{-2}	7.33×10^{-3}	5.51×10^{-3}	2.88×10^{-3}	2.21×10^{-5}
432 ± 5	-22 ± 2	3.74×10^{-2}	1.49×10^{-2}	3.22×10^{-3}	2.49×10^{-3}	1.85×10^{-3}	2.44×10^{-3}	1.25×10^{-4}
	-52 ± 5	7.62×10^{-2}	4.13×10^{-2}	1.13×10^{-2}	3.23×10^{-3}	3.23×10^{-3}	4.17×10^{-3}	1.06×10^{-4}
	-90 ± 9	1.77×10^{-1}	3.55×10^{-2}	1.83×10^{-2}	6.90×10^{-3}	4.75×10^{-3}	4.56×10^{-3}	2.43×10^{-5}

419
420
421

Table 5 Key features of the In-CASE setup

Feature	Numerical value
Collision chamber's parameters	
Height of the collision chamber ($H_{In-CASE}$)	1 m
Distance between droplet injection and AP injection	≈ 10 cm
Diameter of the collision chamber	5 cm
Impaction cup diameter	2.5 cm
AP flowrate in the DMA	Between 0.4 and 1.2 l/min (following the selected AP radius)
Clean air adding at the inlet of the aerosol charger	Between 0.3 and 1.1 l/min (following the selected AP radius)
AP flowrate in the aerosol charger	1.5 l/min

AP flowrate in the collision chamber ($Q_{In-CASE,c}$)	1.5 l/min
Flow velocity in the collision chamber (V_Q)	1.3 cm/s
Flowrate of the upward Argon at the inlet of AP/droplet separator	0.4 l/min
Flowrate of the upward Argon in the impaction cup	1.4 cm/s
AP and Argon flowrate at the outlet of In-CASE chamber (toward the HEPA filter)	1.9 l/min
Air pressure in the collision chamber (P_{air})	1 atm
Temperature in the collision chamber (T_{air})	1.08 ± 0.12 °C
Relative humidity in the collision chamber (RH)	95.1 ± 0.2 %
Duration of experiments (Δt)	From 3 to 6 hours (related to the expected APs mass in droplets)

AP parameters

Selected dry AP radius during experiment (a)	100, 150, 200 or 250 nm
Growth factor of the APs ($GroF$)	Between 1.73 and 1.75 (following the mean levels of relative humidity for the 4 separated AP radii)
Density of sodium fluorescein ($\rho_{fluorescein}$)	$1580 \text{ kg}\cdot\text{m}^{-3}$
Density of the wet APs (ρ_{AP})	$\approx 1110 \text{ kg}\cdot\text{m}^{-3}$
AP terminal velocity	$\leq 10^{-3}$ cm/s (equal to 8×10^{-4} cm/s for the larger selected dry AP radius 250 nm)
AP residence time in the collision chamber	≈ 80 s
Total AP concentration (single and multiple charged at the DMA's outlet)	From 3.10^4 cm^{-3} (for $a=100$ nm and $q = -10 \pm 1 e $) to 2.10^3 cm^{-3} (for $a=250$ nm and $q = -90 \pm 9 e $)
AP charge (q)	From -10 ± 1 to -90 ± 9 elementary charges (following the selected AP radius)

Droplet parameters

Droplet radius (A)	48.5 ± 1.1 μm
Droplet generation frequency (F_d)	25 Hz
Droplet terminal velocity ($U_{A,\infty}$)	≈ 25 cm/s
Number of injected droplets during experiments (N_d)	From 270,000 to 540,000 (related to the expected APs mass in droplets)
Observed distance between two successive droplets	≈ 9 mm ≈ 180 droplet radii
Droplet residence time in the collision chamber	≈ 4 s
Droplet charge (Q)	From $-3.0 \times 10^4 \pm 1.4 \times 10^3$ to $9.6 \times 10^4 \pm 4.3 \times 10^3$ elementary charges
Droplet charge after neutralisation (Q)	0 ± 600 elementary charges

Droplet evaporation between the injection and the end of the collision chamber	$\approx 0.3\%$
Sodium chloride concentration in the pure water	3.3 g/l

422
423
424
425
426
427
428
429
430
431
432
433
434
435
436
437
438
439
440
441
442
443
444
445
446

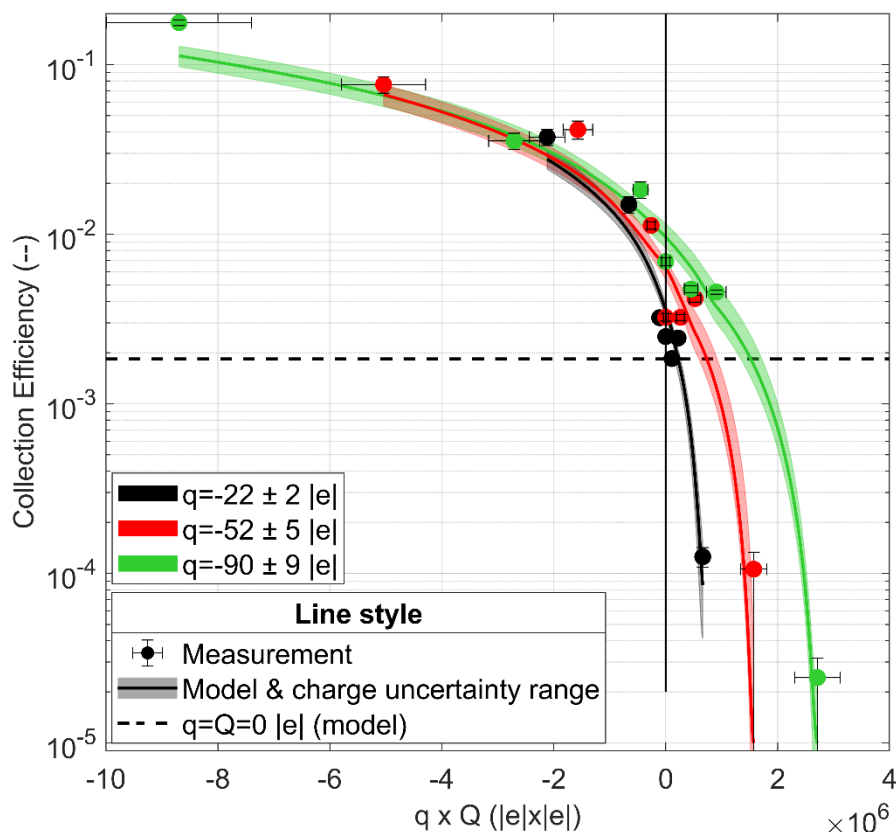
3.2.1 Effect of the product of the droplet and AP charges on the collection efficiency

The CE measurements for a wet AP radius of 432 nm are presented in Figure 7 as a function of the product of the droplet (Q) and AP (q) charges. The measurements are compared to the D  p  e et al. (2019) extended model (solid line) for the 4 AP charges, considering the AP and droplet charge uncertainties. There is a good agreement between model and measurements which indicates that the analytical expression of the electrostatic forces (equation (10)) reliably describes the observations.

Indeed, an important charge influence is measured, increasing or decreasing the CE up to two orders of magnitude for large negative or positive charge products, respectively, compared to the theoretical CE value disregarding the electrostatic effects (dashed line in Figure 7). This is due to the Coulomb inverse square term in the electrostatic forces' equation (10) which dominates - attracting or repelling the APs from the droplet depending on whether the AP and droplet charges have unlike or like signs.

For small positive charge products (approximately $0 \leq q \times Q \leq 10^6 |e| \times |e|$), an increase of CE with a factor of more than three is measured compared to the theoretical CE value without electrostatic forces. This fact truly emphasises the contribution of the short-range attractive term in equation (10) which attracts the APs toward the droplet even though the droplet and AP charges have like signs. Indeed, as previously stated, this term prevails for small charge products (D  p  e et al., 2019).

Note that the same influence of the charge product on the CE is observed for the other three wet AP radii - the CE varies up to four orders of magnitude.



447
448
449
450

Figure 7 CE measurement as a function of the product of the droplet (Q) and AP (q) charges for the wet AP radius of 432 nm and a droplet radius of $48.5 \pm 1.1 \mu\text{m}$. The experimental conditions are summarised in Table 5. Color code informs about the AP charge. The dashed line represents the

451 theoretical CE value disregarding the electrostatic forces (given the air parameters 1 °C, 1 atm, 95%
452 of relative humidity). The solid line is the interpolation of the Dépée et al. (2019) extended model
453 (with the charge uncertainty range) for the respective CE measurements at a given AP charge.

454
455
456
457

3.2.2 Effect of the AP charge on the collection efficiency for a neutral droplet

459

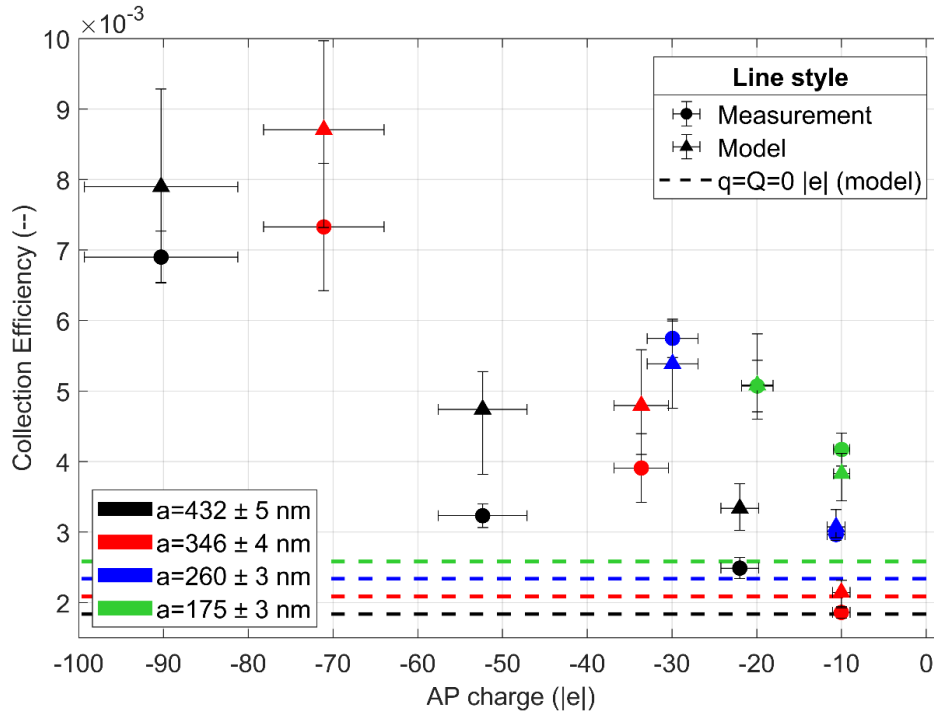
460 In Figure 8, the CE measurements (circle) for a neutral droplet ($Q = 0 \pm 600 |e|$) are presented for
461 the 4 wet AP radii - referred by the color code - with the respective theoretical CE values (triangle).
462 The dashed line represents the theoretical CE value without electrostatic forces.

463 Note that the contribution of the electrostatic forces seems insignificant for an AP charge of about
464 -10 elementary charges and an AP radius of 346 nm and 260 nm as well as an AP of 432 nm with -20
465 elementary charges. Indeed, these measurements are very close to the theoretical ones with no
466 consideration of electrostatic forces. Several microphysical effects have probably an equivalent
467 contribution on the CE measurements such as electrostatic, thermophoretic and diffusiophoretic
468 forces, in addition to AP diffusion, weight and inertia.

469 However, at a given AP radius, an increase of the CE is observed when the number of elementary
470 charges on the APs is larger. Note that this increase appears even though the droplet is neutral (or
471 poorly charged considering the charge uncertainty of 600 elementary charges). For example, given
472 an AP radius of 346 nm, the CE is multiplied by almost a factor 4 when the AP charge increases from
473 -10 to -71 elementary charges. It highlights the contribution of the short-range attractive term in
474 equation (10), showing the presence of a surface charge distribution on the droplet formed by the
475 partial influence of the AP electrostatic field on it. In the current case, this is the only contribution
476 since the droplet is neutral and the Coulomb inverse square term is zero in equation (10). This is an
477 important result since, to our knowledge, there is no experimental observation of the short-range
478 attractive term on the CE in the previous studies of the literature. Here, the good agreement between
479 measured (circle) and modelled (triangle) CEs confirms that the analytical expression of the short-
480 range attractive term in equation (10) is reliable.

481 For a given AP charge, an increase of the CE is measured when the AP radius decreases, probably due
482 to the increase of the electrical mobility of APs. This is in line with the numerical results of Dépée
483 et al. (2019) even though electrostatic effects are not the only contribution involved in this CE
484 increase. Indeed, the Brownian motion of the APs increases for smaller APs and enhances the collision
485 between the droplet and APs.

486 Moreover, the curve slope could be increased for a decrease of the AP radius since the electrical
487 mobility increases but this trend is not visible in Figure 8. It can be due to the uncertainties on the
488 CE measurements, the droplet neutralisation and the AP charge.



489
 490 Figure 8 CE measurement (circle) as a function of the AP charge (q) for the 4 wet AP radii (Color
 491 code). The respective modelled CEs are also presented (triangle). The droplet is neutral with a radius
 492 of $48.5 \pm 1.1 \mu\text{m}$. The experimental conditions are summarised in Table 5. The dashed line represents
 493 the theoretical CE value disregarding the electrostatic forces (given the air parameters 1°C , 1 atm,
 494 95% of relative humidity). The vertical error bars for the modelled CEs consider the AP and droplet
 495 charges uncertainties.

496 3.2.3 Comparison with existing models

497

498 3.2.3.1 Kraemer and Johnstone (1955) prediction

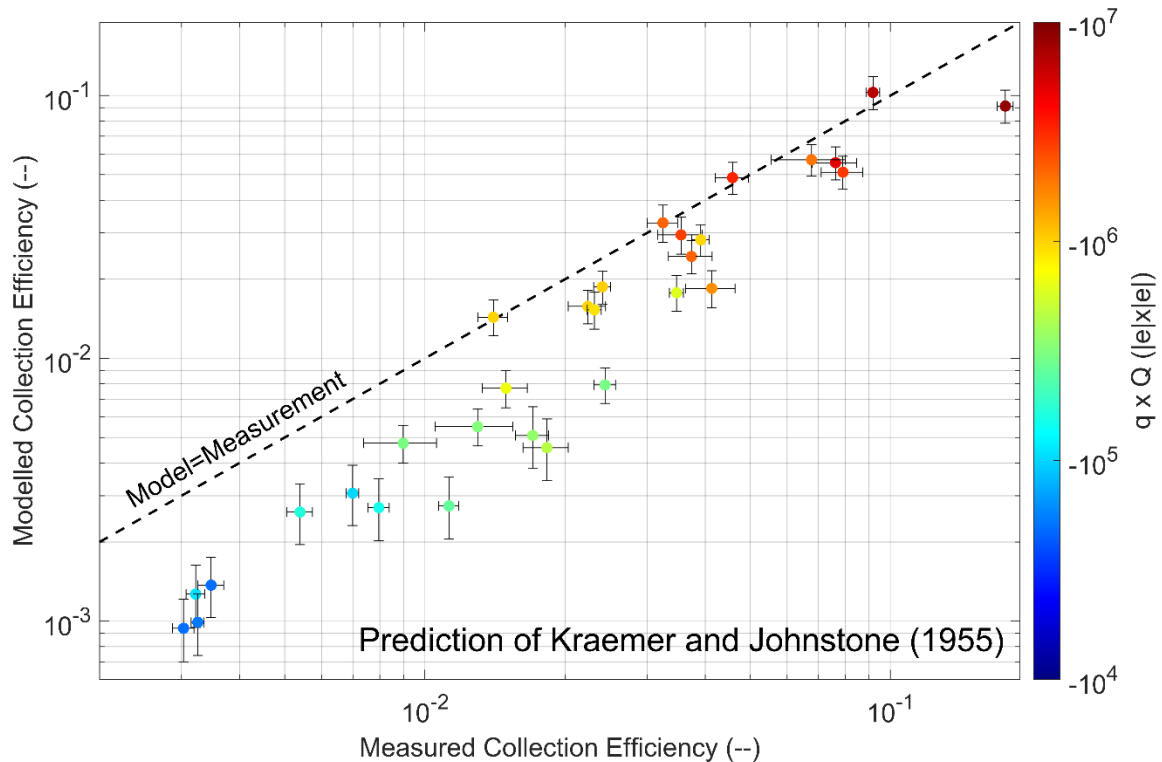
499 To describe the impact of the electric charge on the CE, there is the well-known prediction of
 500 Kraemer and Johnstone (1955), summarised in equation (11):

$$EC_{KJ} = \left(\frac{Q}{\pi \epsilon_0 A^2 \Delta U} \right) \left(\frac{q \times C_u}{6\pi \eta_{air} a} \right) \quad (11)$$

501 With η_{air} - the dynamic viscosity of air, C_u - is the Stokes-Cunningham slip correction factor (defined
 502 in Appendix A of Dépée et al. (2019)) and ΔU the droplet fall velocity relative to the AP fall velocity.
 503 This latter is assumed to be equal to $|U_{A,\infty} - U_{a,\infty}|$ where $U_{a,\infty}$ is the AP settling velocity.

504

505 Since this prediction models the contribution of the attractive Coulomb forces on the CE, only the CE
 506 measurements with a negative charge product for the 4 AP radii are compared. In Figure 9, the
 507 modelled CE from the prediction of Kraemer and Johnstone (1955) as a function of the measured CE
 508 is presented. The horizontal error bars are the measurement uncertainties while the vertical ones
 509 are the extreme theoretical CE values considering the extreme droplet and AP charges (by adding or
 510 subtracting the charge uncertainties). It is shown that the prediction of Kramer and Johnstone (1955)
 511 accurately describes the observation for the large charge products (red color) but the discrepancies
 512 between model and measurement increase when the charge product decreases. Indeed, the less AP
 513 and droplet are electrically charged, the more the model underestimates the CE compared to the
 514 observations. This is due to the formula which only models the attractive Coulomb forces and
 515 disregards the other effects like the AP weight, the AP inertia and the AP diffusion which tend to
 516 increase the CE as well as the diffusiophoretic and the thermophoretic forces (Dépée et al., 2020).
 517 Consequently, the prediction gives better agreement for large charge products where the attractive
 518 Coulomb forces dominate the other effects on the AP collection. This case illustrates the strong
 519 interest of using Lagrangian models like the one of Dépée et al. (2019) which considers all
 520 microphysical effects involved in the in-cloud AP collection and especially their coupling.



521
 522 Figure 9 Modelled CE from the prediction of Kraemer and Johnstone (1955) as a function of the
 523 measured CE. The droplet radius is $48.5 \pm 1.1 \mu\text{m}$. Only the negative charge products for the 4 AP
 524 radii are considered here, represented by the color code. The experimental conditions are
 525 summarised in Table 5.
 526

527 Note that Wang et al. (1983) also compared their CE measurements with this prediction, finding good
 528 agreement since they considered between -10^7 and -10^8 elementary charges on droplets and between
 529 1 and 13.5 elementary charges on APs. So, their charge products were larger than the ones used in
 530 the present study and they had no combined effect - the attractive Coulomb force was by far the
 531 only significant contribution. It can explain why their comparison with the prediction of Kraemer and
 532 Johnstone (1955) are better than the ones presented in Figure 9. Since most of the measurements of
 533 Wang et al. (1983) are for a droplet radius of $250 \mu\text{m}$, they are not comparable to the present ones
 534 which are significantly much smaller ($A = 48.5 \pm 1.1 \mu\text{m}$).
 535

536 3.2.3.2 Dépée et al. (2019) extended model

537 In Figure 10, the modelled CE from the extended model of Dépée et al. (2019) as a function of the
 538 measured CE is presented. The modelled CE are calculated from the experimental parameters (AP
 539 density, air temperature, pressure and relative humidity as well as the sizes and charges) and the CE
 540 values less than 10^{-5} are set to 10^{-5} to avoid an excessive computation time (Dépée et al., 2019). The
 541 horizontal error bars are the measurement uncertainties while the vertical ones are the extreme
 542 theoretical CE values considering the extreme droplet and AP charges (by adding or subtracting the
 543 charge uncertainties). The color code corresponds to the different droplet radii studied.

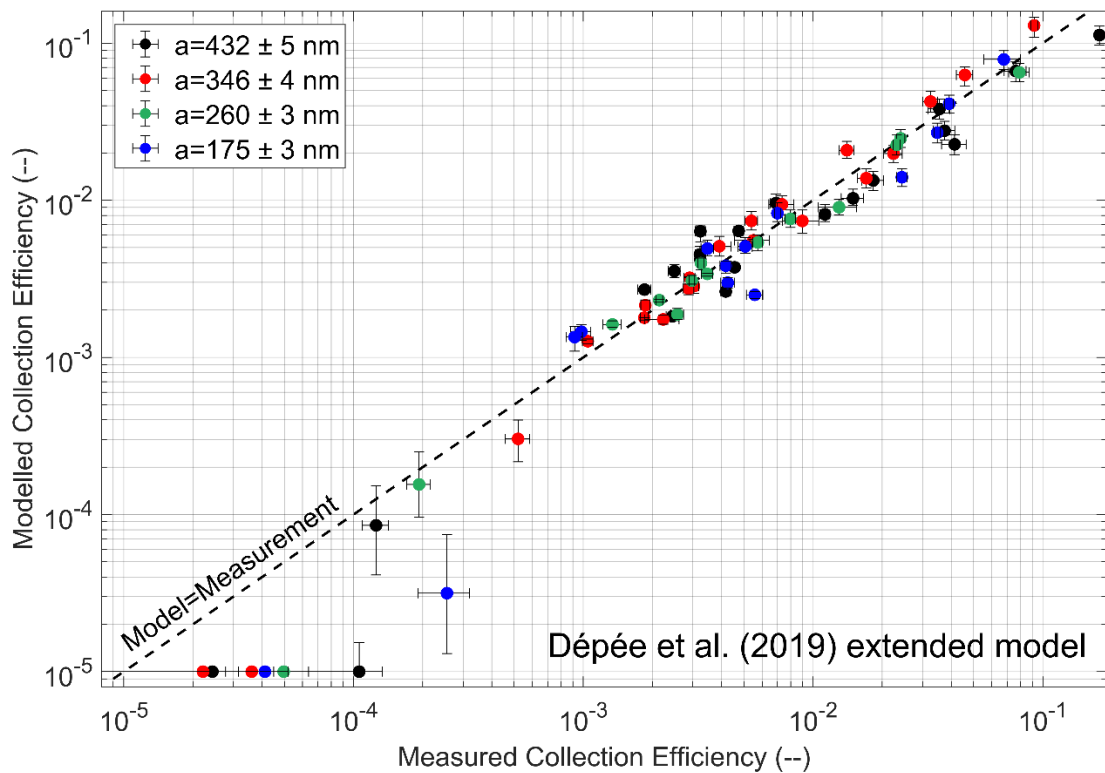
544 A good accordance between the model and the CE measurements are shown. Indeed, it appears that
 545 there are as many data points above the “Model=Measurement” line as below, meaning that the
 546 model overestimates as much as underestimates the observations. Thus, it can be assumed that there
 547 is no missing or unnecessary microphysics effects in the CE modelling. Moreover, the mean difference
 548 between the modelled CEs and the 70 measured CEs is 66 %. This is a reasonable value for a
 549 microphysics parameter such as the collection efficiency which varies on several orders of magnitude,
 550 especially since the value was calculated disregarding the different uncertainties (error bars in
 551 Figure 10) and was as a result over-evaluated.

552 Nevertheless, 6 data points seem inconsistent with discrepancies between model and measurements
 553 from 150 to 1000 %, occurring for the smallest CE values in Figure 10 (lower left). Note that the
 554 discrepancies should be even worse since the modelled CEs, set to 10^{-5} , are actually much lower. By
 555 examining these data points, it appears that the measured AP masses in the droplet impaction cup -
 556 $m_{AP,d}$ in equation (1) - are very close to the detection limit of the spectrometer used. Moreover, for

557 the experimental conditions, the model predicts AP masses in the droplets lower than the detection
558 limit since the Coulomb inverse square term in equation (10) was very repulsive. So, the assumption
559 can be made that a pollution occurred during the various steps of the protocol (end of experiment,
560 disassembly of the chamber's bottom to reach the droplet impaction cup, change of room for the
561 analysis, etc.). Note that the detection limit of the spectrometer is 10^{-15} kg (for the nominal analysis
562 volume considered), which only represents ten APs with a dry radius of 250 nm deposited on the
563 droplet impaction cup. Thus, it exists an important uncertainty in these CE measurements related to
564 a possible contamination. This is difficult to quantify but the low uncertainties of the CE
565 measurements below 10^{-4} were increased in Figure 10. To reduce this potential pollution, it would
566 be necessary to work in a cleanroom or increase the experiment duration to avoid detection problem.
567 However, for these data points the experiment duration was almost 6 hours and, beyond this
568 duration, stability problems of the piezoelectric droplet generator were frequent.

569
570 However, a reasonable agreement between the extended model of Dépée et al. (2019) and the CE
571 measurements are observed. As a reminder, the mean discrepancy was over-evaluated at 66 % which
572 is suitable to describe a microphysical parameter varying on several orders of magnitude for the
573 collection efficiency. Furthermore, if the 6 inconsistent values are removed - the mean discrepancy
574 on the 63 remaining CE measurements decreases from 66 to 38 %.

575
576 The 38 % of discrepancy between the Dépée et al. (2019) extended model and the measurements can
577 be attributed to the dispersion of the AP charge distribution. Indeed, it was not possible to
578 characterize the AP charge distribution which remains an important uncertainty. Moreover, the AP
579 size distribution was assumed to be monodispersed but a dispersion exists, even if very small, which
580 depends on the spectral bandwidth of the DMA. This one can induce some larger (or smaller) APs
581 inside the AP charger which can get an electric charge significantly larger (or smaller) than the
582 predicted one since the charging process is roughly proportional to the AP surface. Then, in the In-
583 CASE chamber, some larger (or smaller) APs with a larger (or smaller) electric charge can interact
584 with the droplets and notably change the final AP mass collected by the droplets during an
585 experiment ($m_{AP,d}$). Another possible explanation is the differences in temperature and relative
586 humidity between the top and the bottom chamber, respectively less than 1°C and 4 % (addressed in
587 **Dépée et al. (2020)**). It could induce local discrepancies during the AP travel time in the chamber in
588 terms of AP density and radius (through the hygroscopicity) or thermophoretic and diffusiophoretic
589 forces which can change the likelihood of being collected by the droplets and then slightly change
590 $m_{AP,d}$. See **Dépée et al. (2020)** for a discussion of the influence of these two latter forces on the CE.
591



592
 593 Figure 10 Modelled CE from the extended model of Dépée et al. (2019) as a function of the measured
 594 CE. The droplet radius is $48.5 \pm 1.1 \mu\text{m}$. The color code refers to the AP radius. The experimental
 595 conditions are summarised in Table 5.
 596

597 CONCLUSION

598 In-CASE (In-Cloud Aerosol Scavenging Experiment) was developed to conduct a series of experiments
 599 evaluating the contribution of microphysical effects on the AP collection by falling cloud droplets.
 600 For this purpose, all the parameters influencing the collection efficiency (CE) are controlled - i.e.
 601 the AP and droplet sizes, the AP and droplet electric charges and the relative humidity. A first
 602 campaign was performed to study the influence of the relative humidity which is the topic of the
 603 Part I (Dépée et al., 2020). This current study was dedicated to a second topic - aiming the impact
 604 of the electric charge on the CE. Furthermore, the CE measurements allow to validate existing models
 605 like the Lagrangian one of Dépée et al. (2019) which considers all microphysical effects involved in
 606 the AP collection by cloud droplets. Indeed, the literature lacks baseline data to get a suitable
 607 comparison with the modelling since most of the previous studies failed to control all parameters
 608 influencing the CE like the AP and droplet sizes and charges as well as the relative humidity (Beard,
 609 1974; Lai et al., 1978; Barlow and Latham, 1983; Byrne and Jennings, 1993). Even though some studies
 610 stand out (Wang and Pruppacher, 1977; Wang et al., 1983), no one examined the influence of the
 611 electrostatic forces when the droplet and AP charges had like signs. Thus, the short-range attractive
 612 term from the analytical expression of the electrostatic forces - equation (10) - used in the current
 613 Lagrangian models (Tinsley and Zhou, 2015; Dépée et al., 2019) has never been experimentally
 614 validated or at least emphasised.

615 In the new CE dataset, the APs and droplets are accurately charged through custom-made droplet
 616 and AP chargers detailed above. Since both charge polarities are found in clouds (Takahashi, 1973),
 617 the droplets were negatively as well as positively charged during experiments. Moreover, several
 618 amounts of elementary charges on the droplet were considered to represent a neutral droplet but
 619 also the weakly and strongly charged droplets respectively found in stratiform and convective clouds
 620 (Takahashi, 1973). The AP charge varied from zero to -90 ± 9 elementary charges depending on the
 621 AP size to represent different amounts of elementary charges encountered in the atmosphere,
 622 particularly the ones of radioactive APs. The relative humidity was maximised in this experimental
 623 work ($95.1 \pm 0.2 \%$) with a mean temperature in the collision chamber ($1.08 \pm 0.12^\circ\text{C}$) stable and
 624 comparable with the other study in the companion paper: Part I (Dépée et al., 2020). Thus, the

625 thermophoretic and diffusiophoretic contributions on the CE measurements were reduced as much
626 as possible. Nevertheless, since Dépée et al. (2020) measured a significant contribution for a
627 comparable relative humidity level, these two forces were still added to the Dépée et al. (2019)
628 model for a reliable model/measurement comparison. Finally, the droplet radius was $48.5 \pm 1.1 \mu\text{m}$
629 and 4 wet AP radii were used - from 175 ± 3 to $432 \pm 5 \text{ nm}$. Note that the hygroscopicity of the sodium
630 fluorescein salt was considered in the calculation of the wet AP radius and the AP density.
631 From the 70 measurements obtained, an influence of the electric charges of 4 orders of magnitude
632 on the CE was observed, strongly increasing or decreasing the CE for large charge products,
633 respectively negative or positive. An increase of the CE was also measured by considering more
634 elementary charges on the APs even though the droplets were neutral (within uncertainties). This
635 observation is an important result since it emphasises the contribution of the short-range attractive
636 term in the electrostatic forces (equation (10)). It validates a surface charge distribution on the
637 droplet, formed by the partial influence of the AP electric field on it, which has never been
638 experimentally shown, to our knowledge, in the literature before.
639 The CE measurements with opposite signs on the droplet and AP were compared to the prediction of
640 Kraemer and Johnstone (1955), giving good agreements for large negative charge products where the
641 Coulomb attractive forces prevail over the other dynamic effects. This is in line with the work of
642 Wang et al. (1983) who also obtained good agreement, considering another droplet radius ($250 \mu\text{m}$)
643 and larger negative charge products. However, in the present study, an increase of the discrepancies
644 between the prediction and the measurement was measured when reducing the number of
645 elementary charges. This is due to the electrostatic forces not being the only effect involved in the
646 AP collection. There is actually a coupling of electrostatic, diffusiophoretic and thermophoretic
647 forces as well as the AP diffusion, weight and inertia. Thus, when the charge product is not strong
648 enough (gets significantly smaller than $10^7 |e|x|e|$), Lagrangian models as the one of Dépée et al.
649 (2019) remain the best estimation of the CE.
650 Finally, the CE measurements were also compared to the extended model of Dépée et al. (2019),
651 showing a really good description of the observed effects. Indeed, the mean discrepancy of the
652 modelling and the 70 measurements was 66 % which is suitable for a microphysical effect varying on
653 several orders of magnitude like the collection efficiency. This value was even better when 6
654 inconsistent measurements, probably contaminated, were disregarded - as it decreases from 66 % to
655 38 %. Moreover, note that the model overestimates as much as underestimates the observations so
656 that the discrepancies probably result from remaining uncertainties (like the dispersion of the AP
657 charge distribution) instead of a missing microphysical effect in the CE modelling.
658 To conclude, 70 new CE measurements are now available that include the influence of the electric
659 charges, showing significant differences with the previous CE measurements and theoretical values
660 from the literature which disregard the electrostatic forces. Thus, it appears to be essential to study
661 the impact of the new baseline data in a cloud-model like DESCAM (Detailed SCAvenging Model,
662 Flossmann, 1985) to examine the influence of the electric charges on the total wet AP removal in the
663 atmosphere. It could strongly affect the atmospheric AP removal since cloud droplets are known to
664 be charged (Takahashi, 1973) as well as the atmospheric AP, even more when APs are radioactive.
665 Indeed, Dépée et al. (2019) estimated that the electric charge of the radioactive APs emitted after
666 the Fukushima accident in 2011 was up to 600 elementary charges. Thus, AP removal could be
667 substantially affected by the electrostatic forces in-cloud and significantly change the ground
668 contamination after a discharge of radioactive materials from a nuclear accident. Since the new
669 Lagrangian model of Dépée et al. (2019) showed an accurate description of the influence of the
670 electric charges (and also of the relative humidity, studied in Part I (Dépée et al. (2020))) on the CE,
671 this latter constitutes a simple, convenient and rapid manner to obtain a CE evaluation for its
672 incorporation in cloud models.
673
674
675
676
677

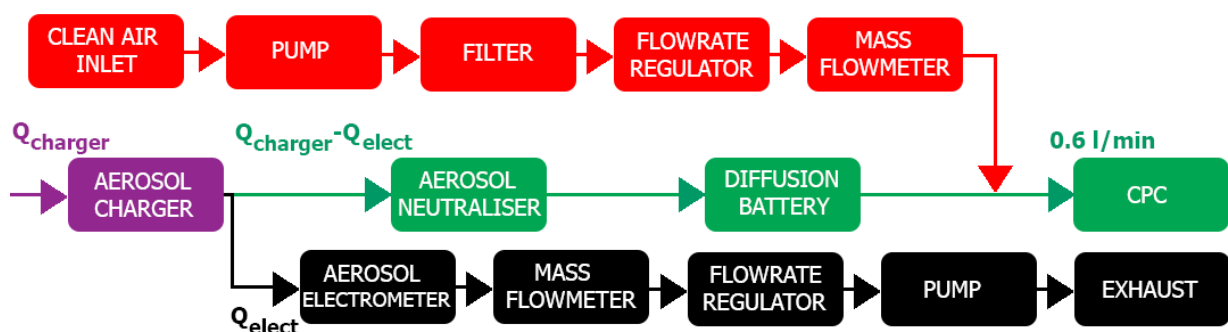
678 Appendix A - AP charger

679 A.1 AP charging relationship's acquisition

680 The AP charging relationships were obtained by performing *ex situ* experiments with the setup
 681 presented in Figure A.1. A nominal AP flow goes through the charger with a monodispersed AP size
 682 distribution. At the charger's outlet, the flow of charged AP is subdivided - 0.6 l/min is directed to a
 683 Condensation Particle Counter (CPC; TSI 3787) to deduce the concentration number of AP in the
 684 charger ($C_{N,AP}$) while the other part goes toward an electrometer (TSI 3068A) to measure the current
 685 (I_{elect}) due to the charge evacuation. Before entering the CPC, APs are neutralised to avoid any
 686 deposition on the metallic walls of the CPC and then the AP flow passes through a diffusion battery
 687 to filter the fine particles produced during the discharges inside the charger. The mean AP charge
 688 ($\langle q \rangle$) was then calculated from the equation (A.1) with the elementary charge (e) and the AP flowrate
 689 in the electrometer (Q_{elect}):

$$\langle q \rangle = \frac{I_{elect}}{e \times C_{N,AP} \times Q_{elect}} \quad (\text{A.1})$$

690 Several AP flowrates in the charger ($Q_{charger}$) were considered to study the AP penetration. When
 691 $Q_{charger}$ was less than 0.7 l/min, clean air was added before the CPC to maintain a CPC flowrate of
 692 0.6 l/min - this part is presented in red in Figure A.1. From these experiments, it was found that
 693 $Q_{charger}=1.5$ l/min maximises the AP penetration through the charger. Note that the AP penetration
 694 is defined, at the charger's outlet, as the AP number concentration when the charger is switched on
 695 over the AP number concentration when this latter is switched off.



696

697 Figure A.1 Setup to obtain the AP charging relationship. The red dashed rectangle is the part added
 698 to study the AP penetration through the charger.

699

700 A.2 Validation

701 The setup (Figure A.1) was conducted with the charger turned off to measure the mean AP charge
 702 after the DMA. It was found one elementary charge on APs which validates that the multiple charged
 703 APs are stopped at the DMA's inlet by the aerodynamic impactor. Thus, the assumption made that
 704 the AP size distribution is monodispersed after the DMA is justified. The AP charge was also analysed
 705 during 5 hours - no AP charge modification was measured over time. Moreover, the saturated AP
 706 charges visible in Figure 4 for a tungsten wire potential less than -12.5 kV was also compared to the
 707 theoretical values of Pauthenier and Moreau-Hanot (1932) - giving a good agreement.

708 Note that two other characterizations were made during these *ex situ* experiments like the
 709 determination of the ion current between the grounded cylinder and the tungsten wire (Figure 3) or
 710 the discharge frequencies - these both parameters are related to the tungsten wire potential. These
 711 curves were used to precisely identify the discharge regime of the charger (Unger, 2001) - the
 712 negative Trichel regime which provides a large discharge frequency and then a spatially homogeneous
 713 particle charging around the tungsten wires.

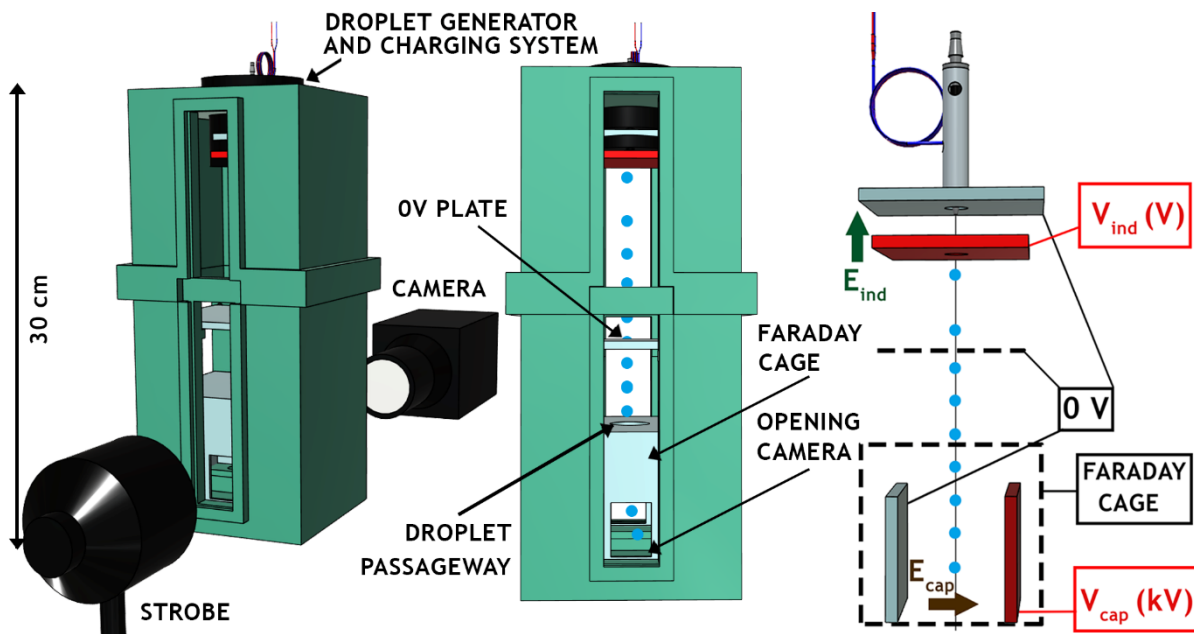
714

715

716 **Appendix B - Droplet charging relationship obtention**

717 **B.1 Overview**

718 Figure B.1 presents the setup used in *ex situ* experiments to measure the droplet charge where the
 719 charging relationship in Figure 6 comes from. The housing made with a 3D printer - containing the
 720 droplet injector and the charging system (detailed in section 1.5) - is set above a capacitor composed
 721 of one neutral potential plate and another plate connected to a high potential (V_{cap}). In this latter,
 722 pictures are obtained by optical shadowgraphy to get the droplet trajectories. The electric field
 723 (E_{cap}) induced in the capacitor disturbs the droplet motion according to its electric charge. Thus, the
 724 droplet charge is evaluated by finding the one which fits the best the theoretical droplet trajectory
 725 - deduced from the 2nd Newton's law - and the measured droplet trajectories. A Faraday cage ensures
 726 the electric field at the capacitor (E_{cap}) has no effect on the electric field at the electrostatic
 727 inductor (E_{ind}). Since this is not a proper Faraday cage because of the holes for droplets and camera,
 728 a horizontal metallic perforated plate is added below the droplet generator housing and connected
 729 to the neutral potential to prevent the electric field (E_{cap}) from changing the droplet charge.
 730



731
 732 Figure B.1 Setup to obtain the droplet charging relationship - (Left and Center) 3D view and (Right)
 733 schema (not at scale)
 734

735 **B.2 Droplet charge evaluation**

736 A series of 200 pictures pairs, with each one dephased from the other by a known time-step (Δt), are
 737 obtained by optical shadowgraphy at the level of the capacitor. A circle Hough transform is then
 738 applied to evaluate the droplet centers in every picture - an example is given in Figure B.2 (Left)
 739 where the two droplets from a picture are represented by two black crosses meanwhile the blue cross
 740 is the detected droplet from the coupled picture dephased by Δt .
 741

742 Then, the instantaneous droplet velocity $\overline{U_{D_0}}(t) = U_{D_0,x} \overline{u_x} + U_{\infty,A} \overline{u_y}$ at the first detected droplet
 743 position (D_0) of coordinates (x_{D_0}, y_{D_0}) is calculated and the vertical velocity component ($U_{\infty,A}$)
 744 determines the droplet radius (A) by reversing the Beard (1976) model. Here, the circle Hough
 745 transform is not used to calculate the droplet radius like during CE experiments - see Figure 8, right
 746 from part I, Dépée et al. (2020). Indeed, the camera zoom is at the lowest to get a large field - the
 747 uncertainty would be too large.
 748

749 Finally, the theoretical droplet trajectories at the capacitor are deduced by solving the 2nd Newton's
 750 law where the buoyancy force (F_{buoy}), the drag force (F_{Drag}) and the electrostatic force ($F_{E_{cap}}$)
 751 related to the electric field (E_{cap}) at the capacitor are considered, summarised in equations (B.1) :
 752

$$\begin{cases} m_D \frac{d\mathbf{U}_D(t)}{dt} = \mathbf{F}_{buoy} + \mathbf{F}_{Drag} + \mathbf{F}_{E_{cap}} \\ \mathbf{F}_{buoy} = -m_D \frac{\rho_{water} - \rho_{air}}{\rho_{water}} g \mathbf{u}_y \\ \mathbf{F}_{Drag} = -\frac{C_D \pi \rho_{air} U_D^2 A^2}{2} \frac{\mathbf{U}_D(t)}{\|\mathbf{U}_D(t)\|} \\ \mathbf{F}_{E_{cap}} = Q E_{cap} \mathbf{u}_x \end{cases} \quad (\text{B.1})$$

753 With \mathbf{U}_D - the instantaneous droplet velocity vector at the computational time t , ρ_{air} and ρ_{water} -
 754 the air and water densities, g - the acceleration of gravity, m_D - the droplet mass, Q - the droplet
 755 charge, C_D - the drag coefficient, \mathbf{u}_x and \mathbf{u}_y - the unit vectors in the cartesian coordinate system
 756 visible in Figure B.2 (Left).

757
 758 By projecting on the corresponding axis, it is obtained the system of equations (B.2) to solve:

$$\begin{cases} m_D \frac{dU_{D,x}(t)}{dt} = QE_{cap} - \frac{C_{D,x} \pi \rho_{air} U_{D,x}^2 A^2}{2} \\ m_D \frac{dU_{D,y}(t)}{dt} = -m_D \frac{\rho_{water} - \rho_{air}}{\rho_{water}} g - \frac{C_{D,y} \pi \rho_{air} U_{D,y}^2 A^2}{2} \end{cases} \quad (\text{B.2})$$

759 Where $C_{D,x}$ and $C_{D,y}$ are the drag coefficient projections depending on the Reynolds number
 760 projections Re_x et Re_y in the cartesian coordinate system. Since $Re_x \ll 1$ et $Re_y < 2$ in the study, the
 761 drag coefficient projections are calculated from the analytical expression given by Hinds (2012) and
 762 summarised in equations (B.3):

$$\begin{cases} C_{D,x} = \frac{24}{Re_x} = \frac{12 \eta_{air}}{AU_{D,x} \rho_{air}} \\ C_{D,y} = \frac{24}{Re_y} \underbrace{(1 + 0,15 Re_y^{0,687})}_{\textcircled{1}} \approx \frac{12 \eta_{air}}{AU_{D,y} \rho_{air}} \underbrace{\left(1 + 0,15 \left(\frac{2AU_{\infty,A} \rho_{air}}{\eta_{air}}\right)^{0,687}\right)}_{=K_1} \end{cases} \quad (\text{B.3})$$

763 Note that the term $\textcircled{1}$ in the Equations (B.3) is supposed as constant to simplify the resolution of the
 764 equations (B.1) - giving second order differential equations. This assumption is justified since Re_y is
 765 close to the unity and then $C_{T,y} = \frac{24}{Re_y}$ remains suitable. The equation system to solve becomes,
 766 equations (B.4):

$$\begin{cases} m_D \frac{dU_{D,x}(t)}{dt} = QE_{cap} - \frac{K_2}{6\pi A \eta_{air}} U_{D,x} \\ m_D \frac{dU_{D,y}(t)}{dt} = -m_D \frac{\rho_{water} - \rho_{air}}{\rho_{water}} g - \frac{6\pi A \eta_{air} K_1}{K_3} U_{D,y} \end{cases} \quad (\text{B.4})$$

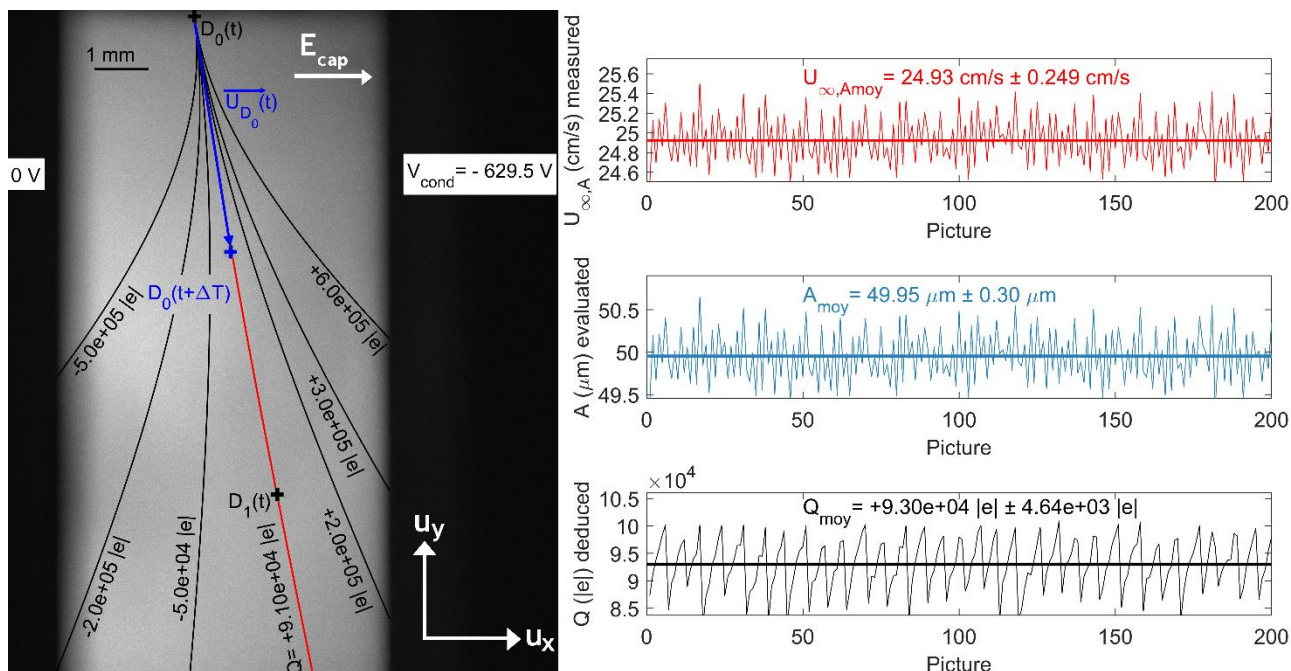
767 After two consecutive integrations with the initial conditions - $U_{D,x}(t=0) = U_{D_0,x}$, $U_{D,y}(t=0) = U_{\infty,A}$,
 768 $(x_D(t=0), y_D(t=0)) = (x_{D_0}, y_{D_0})$, the analytical equations of the horizontal and vertical droplet
 769 positions, respectively referred as x_{th} and y_{th} , are given in equations (B.5):

$$\begin{cases} x_{th}(t) = \frac{Q E_{cap}}{K_2} t + \frac{m_D}{K_2} \left(U_{D_0,x} - \frac{Q E_{cap}}{K_2} \right) \left[1 - e^{-\frac{K_2}{m_D} t} \right] + x_{D_0} \\ y_{th}(t) = -\frac{m_D (\rho_{water} - \rho_{air})}{K_3 \rho_{water}} g t + \frac{m_D}{K_3} \left(U_{\infty,A} + \frac{m_D (\rho_{water} - \rho_{air})}{K_3 \rho_{water}} g \right) \left[1 - e^{-\frac{K_3}{m_D} t} \right] + y_{D_0} \end{cases} \quad (\text{B.5})$$

771 Where $E_{cap} = -grad(V) = -\frac{V_{cap}}{0,01} \mathbf{V}/m$.

772
 773 As presented in Figure B.2 (Left), for every pair of pictures, the droplet charge (Q) is then evaluated
 774 by looking for the theoretical droplet trajectory from the Equations (B.5) which fits the best with the
 775 observed droplet positions. In the given example (Figure B.2, Left), the fitted theoretical trajectory
 776 - for $V_{ind} = -32.25 \text{ V}$, $V_{cap} = -629.5 \text{ V}$, $A = 49.5 \text{ }\mu\text{m}$ and the air temperature $T_{air} = 292.55 \text{ K}$ - illustrated
 777 by the red line is obtained for a droplet charge (Q) of $+9.10e+04 |e|$. Finally, this method is applied

778 for the 200 picture pairs to get the mean droplet charge value - visible in Figure B.2 (Right). Note
 779 that the standard deviation of the 200 Q values gives the error bars in Figure 6.
 780



781
 782 Figure B.2 (Left) Determination of the theoretical droplet trajectory which fits the best with the
 783 observed droplet positions - red line - and deduction of the droplet charge (Q). In this example,
 784 $V_{ind} = -32.25$ V, $V_{cap} = -629.5$ V, $A = 49.5$ μm and the air temperature $T_{air} = 292.55$ K. (Right, Top)
 785 Terminal velocity measurement, (Right, Middle) Droplet radius evaluation by reversing the Beard
 786 (1976) model and (Right, Bottom) droplet charge deduction for a series of 200 pictures pairs. Mean
 787 and standard deviations for the corresponding parameters are presented.

788
 789 **B.3 Validation**

790 The method presented at the previous section is possible as long as the droplet has reached its
 791 terminal velocity. As mentioned in **Dépée et al. (2020)** and visible in Figure 8 (Left) of the same
 792 paper, droplets are generated at a velocity larger than their terminal velocity. It has been found that
 793 a distance between the droplet generator and the capacitor of 15 cm was large enough to allow
 794 droplets to reach their terminal velocity. In the setup in Figure B.1, this requirement prevails.

795
 796 An experiment was performed to ensure that reversing the Beard (1976) model was a suitable method
 797 to evaluate the droplet radius. For this purpose, the same droplet train was recorded in optical
 798 shadowgraphy with a camera zoom at the lowest and at the greatest to respectively apply the Beard
 799 (1976) model inversion and the circle Hough transform. In all tests, it was found a discrepancy of less
 800 than 2 % between the two methods, giving overvaluations as well as undervaluations when comparing
 801 one to the other.

802 Also, the disturbance of the electric field at the capacitor (E_{cap}) on the vertical droplet velocity was
 803 studied. E_{cap} was then turned on and off to investigate the change in vertical droplet velocity. It was
 804 found that during tests, E_{cap} reduced the vertical velocity up to 1.3 %. This situation was for a droplet
 805 charge (Q) and a capacitor potential (V_{cap}) both negative. Some other tests also showed that the
 806 droplet vertical velocity was increased up to 0.3 %, for a droplet charge and a capacitor potential of
 807 unlike sign. Since these two extreme cases respectively represent an undervaluation of less than
 808 0.7 % and an overestimation of less than 0.2 % of the droplet radius - this effect was neglected.

809 Finally, two other validations can be formulated by examining Figure 6. First, several capacitor
 810 potentials (V_{cap}) were used in the tests - from -629.5 to -477.4 V - giving the same charging
 811 relationship. The Faraday Cage is consequently reliable, there is no impact of the electric field
 812 (E_{cap}) on the droplet charge. Secondly, in the four tests the droplet radius varies from 47.0 to
 813 51.2 μm . Thus, the droplet charging system is independent of the droplet size and droplet
 814 evaporation.

815 **References**

816 Ardon-Dryer, K., Huang, Y. W., and Cziczo, D. J.: Laboratory studies of collection efficiency of sub-
817 micrometer aerosol particles by cloud droplets on a single-droplet basis, 2015.
818
819 Barlow, A. K., and Latham, J.: A laboratory study of the scavenging of sub-micron aerosol by charged
820 raindrops. *Quarterly Journal of the Royal Meteorological Society*, 109(462), 763-770, 1983.
821
822 Beard, K. V.: Experimental and numerical collision efficiencies for submicron particles scavenged by
823 small raindrops. *Journal of the Atmospheric Sciences*, 31(6), 1595-1603, 1974.
824
825 Beard, K. V. (1976). Terminal velocity and shape of cloud and precipitation drops aloft. *Journal of the*
826 *Atmospheric Sciences*, 33(5), 851-864.
827
828 Byrne, M. A., and Jennings, S. G. (1993). Scavenging of sub-micrometre aerosol particles by water
829 drops. *Atmospheric Environment. Part A. General Topics*, 27(14), 2099-2105.
830
831 Cherrier, G., Belut, E., Gerardin, F., Tanière, A., and Rimbert, N. Aerosol particles scavenging by a
832 droplet: Microphysical modeling in the Greenfield gap. *Atmospheric environment*, 166, 519-530, 2017.
833
834 Chate, D. M., and Pranesha, T. S. Field studies of scavenging of aerosols by rain events. *Journal of*
835 *Aerosol Science*, 35(6), 695-706, 2004.
836
837 Clement, C. F., and Harrison, R. G.: The charging of radioactive aerosols. *Journal of aerosol science*,
838 23(5), 481-504, 1992.
839
840 Davenport, H. M., and Peters, L. K. Field studies of atmospheric particulate concentration changes
841 during precipitation. *Atmospheric Environment* (1967), 12(5), 997-1008, 1978.
842
843 Dépée, A., Lemaitre, P., Gelain, T., Mathieu, A., Monier, M., and Flossmann, A. Theoretical study of
844 aerosol particle electroscavenging by clouds. *Journal of Aerosol Science*, 135, 1-20, 2019.
845
846 **Dépée, A., Lemaitre, P., Gelain, T., Monier, M., and Flossmann, A.: Laboratory study of collection**
847 **efficiency of submicron aerosol particles by cloud droplets. Part I - Influence of relative**
848 **humidity. Submitted to Atmospheric Chemistry and Physics,**
849 **<https://acp.copernicus.org/preprints/acp-2020-831>, 2020.**
850
851 Dockery, D. W., Schwartz, J., and Spengler, J. D.: Air pollution and daily mortality: associations with
852 particulates and acid aerosols. *Environmental research*, 59(2), 362-373, 1992.
853
854 Depuydt, G. Etude expérimentale in situ du potentiel de lessivage de l'aérosol atmosphérique par les
855 précipitations (Doctoral dissertation), 2013.
856
857 Flossmann, A. I., Hall, W. D., and Pruppacher, H. R. A theoretical study of the wet removal of
858 atmospheric pollutants. Part I: The redistribution of aerosol particles captured through nucleation and
859 impaction scavenging by growing cloud drops. *Journal of the Atmospheric Sciences*, 42(6), 583-606,
860 1985.
861
862 Flossmann, A. I. Interaction of aerosol particles and clouds. *Journal of the atmospheric sciences*, 55(5),
863 879-887, 1998.
864
865 Greenfield, S. M.: Rain scavenging of radioactive particulate matter from the atmosphere. *Journal of*
866 *Meteorology*, 14(2), 115-125, 1957.
867
868 Grover, S. N., and Beard, K. V.: A numerical determination of the efficiency with which electrically
869 charged cloud drops and small raindrops collide with electrically charged spherical particles of various
870 densities. *Journal of the Atmospheric Sciences*, 32(11), 2156-2165, 1975.
871

872 Grover, S. N., Pruppacher, H. R., and Hamielec, A. E.: A numerical determination of the efficiency with
873 which spherical aerosol particles collide with spherical water drops due to inertial impaction and phoretic
874 and electrical forces. *Journal of the Atmospheric Sciences*, 34(10), 1655-1663, 1977.
875
876
877 Hinds, W. C.: *Aerosol technology: properties, behavior, and measurement of airborne particles*. John
878 Wiley and Sons, 2012.
879
880 Jackson, J. D.: *Classical Electrodynamics*, 1999.
881
882 Jaenicke, R.: Tropospheric aerosols. In *International Geophysics* (Vol. 54, pp. 1-31). Academic Press,
883 1993.
884
885 Jaworek, A., Adamiak, K., Balachandran, W., Krupa, A., Castle, P., and Machowski, W.: Numerical
886 simulation of scavenging of small particles by charged droplets. *Aerosol Science and Technology*,
887 36(9), 913-924, 2002.
888
889 Kerker, M., and Hampl, V.: Scavenging of Aerosol Particles by a Falling Water Drop and Calculation of
890 Washout Coefficients. *Journal of the Atmospheric Sciences*, 31(5), 1368-1376, 1974.
891
892 Kraemer, H. F., and Johnstone, H. F.: Collection of aerosol particles in presence of electrostatic fields.
893 *Industrial and Engineering Chemistry*, 47(12), 2426-2434.
894
895 Ladino, L., Stetzer, O., Hattendorf, B., Günther, D., Croft, B., and Lohmann, U.: Experimental study of
896 collection efficiencies between submicron aerosols and cloud droplets. *Journal of the Atmospheric
897 Sciences*, 68(9), 1853-1864, 2011.
898
899 Laguionie, P., Roupsard, P., Maro, D., Solier, L., Rozet, M., Hébert, D., and Connan, O.: Simultaneous
900 quantification of the contributions of dry, washout and rainout deposition to the total deposition of
901 particle-bound ⁷Be and ²¹⁰Pb on an urban catchment area on a monthly scale. *Journal of Aerosol
902 Science*, 77, 67-84, 2014.
903
904 Lai, K. Y., Dayan, N., and Kerker, M.: Scavenging of aerosol particles by a falling water drop. *Journal
905 of the Atmospheric Sciences*, 35(4), 674-682, 1978.
906
907 Laakso, L., Grönholm, T., Rannik, Ü., Kosmale, M., Fiedler, V., Vehkamäki, H., and Kulmala, M.:
908 Ultrafine particle scavenging coefficients calculated from 6 years field measurements. *Atmospheric
909 Environment*, 37(25), 3605-3613, 2003.
910
911 Lemaitre, P., Querel, A., Monier, M., Menard, T., Porcheron, E., and Flossmann, A. I.: Experimental
912 evidence of the rear capture of aerosol particles by raindrops. *Atmospheric Chemistry and Physics*,
913 17(6), 2017.
914
915 Lemaitre, P., Sow, M., Quérel, A., Dépée, A., Monier, M., Menard, T., and Flossmann, A.I. : Contribution
916 of Phoretic and Electrostatic Effects to the Collection Efficiency of Submicron Aerosol Particles by
917 Raindrops. *Atmosphere*, 11(10), 1028, 2020.
918
919 Lira, I.: *Evaluating the measurement uncertainty: fundamentals and practical guidance*, 2003.
920
921 Pauthenier, M., and Moreau-Hanot, M.: *La charge des particules sphériques dans un champ ionisé*,
922 1932.
923
924 Pranesha, T. S., and Kamra, A. K.: Scavenging of aerosol particles by large water drops: 1. Neutral
925 case. *Journal of Geophysical Research: Atmospheres*, 101(D18), 23373-23380, 1996.
926
927 Pruppacher, H. R., and Klett, J. D.: *Microphysics of Clouds and Precipitation*.
928 (Dordrecht/Boston/London), 1997.
929

930 Quérel, A., Lemaitre, P., Monier, M., Porcheron, E., Flossmann, A. I., and Hervo, M.: An experiment to
931 measure raindrop collection efficiencies: influence of rear capture. *Atmospheric Measurement*
932 *Techniques*, 7(5), 1321-1330, 2014.

933

934 Reischl, G. P. W. W., John, W., and Devor, W.: Uniform electrical charging of monodisperse
935 aerosols. *Journal of Aerosol Science*, 8(1), 55-65, 1977.

936

937 Santachiara, G., Prodi, F., and Belosi, F.: A review of termo-and diffusio-phoresis in the atmospheric
938 aerosol scavenging process. Part 1: Drop scavenging, 2012.

939

940 Slinn, W. G. N., and Hales, J. M.: A reevaluation of the role of thermophoresis as a mechanism of in-
941 and below-cloud scavenging. *Journal of the Atmospheric Sciences*, 28(8), 1465-1471, 1971.

942

943 Slinn, W. G.: Precipitation scavenging: some problems, approximate solutions and suggestions for
944 future research (No. BNWL-SA-5062). Battelle Pacific Northwest Labs., Richland, Wash, USA, 1974.

945

946 Slinn, W. G. N.: Some approximations for the wet and dry removal of particles and gases from the
947 atmosphere. *Water, Air, and Soil Pollution*, 7(4), 513-543, 1977.

948

949 Twomey, S. Pollution and the planetary albedo. *Atmospheric Environment (1967)*, 8(12), 1251-1256,
950 1974.

951

952 Takahashi, T. Measurement of electric charge of cloud droplets, drizzle, and raindrops. *Reviews of*
953 *Geophysics*, 11(4), 903-924, 1973.

954

955 Tinsley, B. A., Rohrbaugh, R. P., Hei, M., and Beard, K. V.: Effects of image charges on the scavenging
956 of aerosol particles by cloud droplets and on droplet charging and possible ice nucleation processes.
957 *Journal of the atmospheric sciences*, 57(13), 2118-2134, 2000.

958

959 Tinsley, B. A., Zhou, L., and Plemmons, A. Changes in scavenging of particles by droplets due to weak
960 electrification in clouds. *Atmospheric Research*, 79(3), 266-295, 2006.

961

962 Tinsley, B. A., and Zhou, L.: Parameterization of aerosol scavenging due to atmospheric
963 ionization. *Journal of Geophysical Research: Atmospheres*, 120(16), 8389-8410, 2015.

964

965 Unger, L.: *Charge d'aérosol par décharge électrique pour la filtration d'effluents particuliers* (Doctoral
966 dissertation, Paris 11), 2001.

967

968 Unger, L., Boulaud, D., and Borra, J. P.: Unipolar field charging of particles by electrical discharge:
969 effect of particle shape. *Journal of Aerosol Science*, 35(8), 965-979, 2004.

970

971 Vohl, O., Mitra, S. K., Wurzler, S., Diehl, K., and Pruppacher, H. R.: Collision efficiencies empirically
972 determined from laboratory investigations of collisional growth of small raindrops in a laminar flow field.
973 *Atmospheric research*, 85(1), 120-125, 2007.

974

975 Volken, M., and Schumann, T.: A critical review of below-cloud aerosol scavenging results on Mt. Rigi.
976 *Water, Air, and Soil Pollution*, 68(1-2), 15-28, 1993.

977

978 Wang, P. K., and Pruppacher, H. R.: An experimental determination of the efficiency with which aerosol
979 particles are collected by water drops in subsaturated air. *Journal of the Atmospheric Sciences*, 34(10),
980 1664-1669, 1977.

981

982 Wang, P. K., Grover, S. N., and Pruppacher, H. R.: On the effect of electric charges on the scavenging
983 of aerosol particles by clouds and small raindrops. *Journal of the Atmospheric Sciences*, 35(9), 1735-
984 1743, 1978.

985

986 Wang, H. C., Leong, K. H., Stukel, J. J., and Hopke, P. K.: Collection of hydrophilic and hydrophobic
987 charged submicron particles by charged water droplets. *Journal of aerosol science*, 14(6), 703-712,
988 1983.

989

990 Young, K. C.: The role of contact nucleation in ice phase initiation in clouds. *Journal of the Atmospheric*
991 *Sciences*, 31(3), 768-776, 1974.
992